Chapter 4

Microstructure Evolution in Ultrafine-grained Magnesium Alloy AZ31 Processed by Severe Plastic Deformation

Jitka Stráská, Josef Stráský, Peter Minárik, Miloš Janeček and Robert Král

Additional information is available at the end of the chapter

http://dx.doi.org/10.5772/61611

Abstract

Commercial MgAlZn alloy AZ31 was processed by two techniques of severe plastic deformation (SPD): equal channel angular pressing and high pressure torsion. Several microscopic techniques, namely light, scanning and transmission electron microscopy, electron backscatter diffraction, and automated crystallographic orientation mapping were employed to characterize the details of microstructure evolution and grain fragmentation of the alloy as a function of strain imposed to the material using these SPD techniques. The advantages and drawbacks of these techniques, as well as the limits of their resolution, are discussed in detail. The results of microstructure observations indicate the effectiveness of grain refinement by severe plastic deformation in this alloy. The thermal stability of ultrafine-grained structure that is important for practical applications is also discussed.

Keywords: Magnesium, ECAP, HPT, grain refinement, thermal stability

1. Introduction

Due to its low density, magnesium alloys are very attractive materials for structural components in automotive, aerospace and other transport industries with the potential to replace steel or aluminium alloys in various applications [1]. Nevertheless, the use of magnesium alloys in more complex applications is limited because of the problems associated with poor corrosion and creep resistance and above all the low ductility. The limited ductility is a consequence of the hexagonal structure providing the lack of independent slip systems and the large difference in the values of the critical resolved shear stress in different slip systems.

Moreover, the strong deformation textures and stress anisotropy in magnesium alloys reduces significantly the variety of possible industrial applications.

The mechanical and other essential properties determining the application of magnesium alloys may be improved by refining the grain size to the submicrocrystalline or even nanocrystalline level. In the last three decades, a variety of new techniques have been proposed for the production of the ultra-fine grain (UFG) structures in materials. The common feature of all these techniques is the imposition of large straining and consequent introduction of very high density of lattice defects in the material resulting in exceptional grain refinement. Since these procedures introduce severe plastic deformation (SPD) to bulk solids, it became convenient to describe all of them as SPD processing. Several processes of SPD are now available but only two of them receiving the most attention at present time, in particular, equal channel angular pressing (ECAP) and high-pressure torsion (HPT) [2–5].

The practical applications of the UFG materials are limited due to low microstructure stability at elevated temperatures that complicates the processing of final products. Thermal stability depends on many variables, such as stacking fault energy of the material, processing, or properties of grain boundaries [6]. Microstructure stability can be improved by various alloying elements or composite reinforcements.

In order to understand the microscopic mechanisms of grain fragmentation during SPD processing, detailed characterization of the microstructure is needed. The objective of this review paper is to employ a wide variety of standard and enhanced microscopic techniques to characterize the microstructure evolution of the UFG magnesium alloy AZ31 by employing several microscopic techniques, in particular, light microscopy, scanning electron microscopy (SEM), transmission electron microscopy (TEM), electron backscatter diffraction (EBSD), and a new sophisticated microscopic method—automated crystallographic orientation mapping in a TEM (ACOM-TEM).

2. Experiment

The commercial magnesium alloy AZ31 (3 wt. % of Al, 0.8 wt. % of Zn, and 0.2 wt. % of Mn) was used in this investigation. Two most popular techniques of severe plastic deformation were employed for material processing and microstructure refinement, namely equal-channel angular pressing preceded by hot extrusion (EX-ECAP) and high-pressure torsion (HPT).

2.1. Equal-channel angular pressing

Equal-channel angular pressing (ECAP) is one of the most developed and also commercially used SPD procedures. ECAP was invented by Segal et al. in the 1970s and 1980s in the former Soviet Union [7]. Since its invention, ECAP has become well-known and widely used technique. Nowadays, ECAP is a commonly used SPD method applicable in many branches of industries. The main advantage of the ECAP technique is the same cross-sectional dimensions of the specimens before and after pressing. This fact allows repetitive pressing and the accumulation of strain in the specimen. Furthermore, the ECAP is a quite simple process commonly used worldwide.

The ECAP die consists of two channels with the same cross-section. Generally, the ECAP die is characterized by two angles: *Φ*, which is formed by these two channels, and the angle *Ψ* that indicates the outer arc of curvature at the intersection of the two channels (see Figure 1).

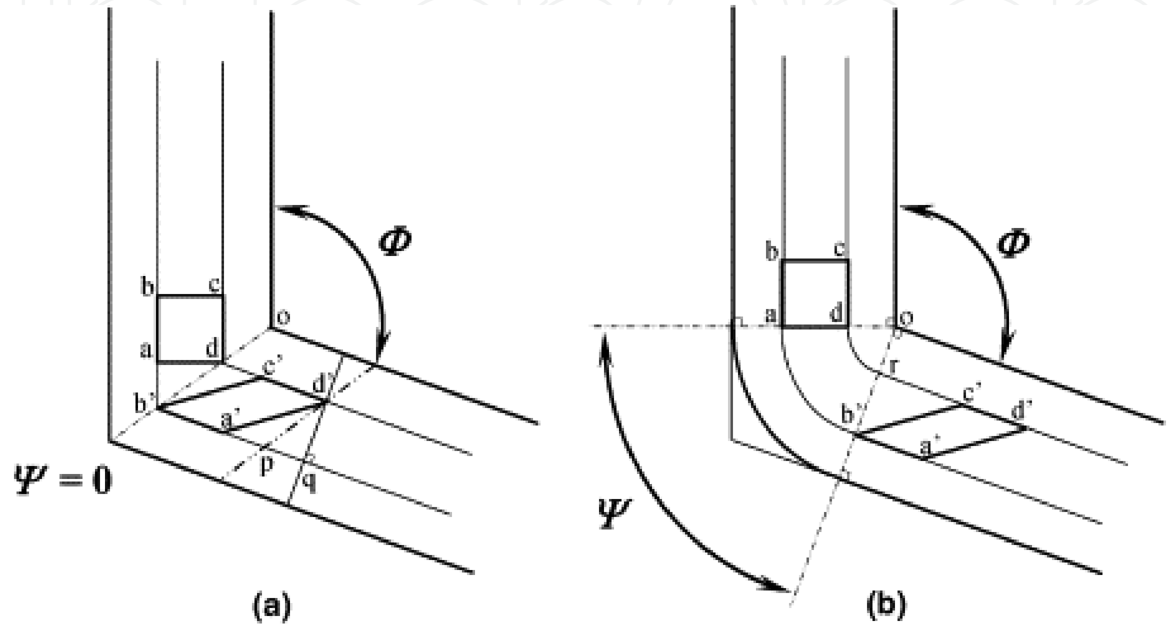

Figure 1. The scheme of pressing of the rectangular sample with the square cross-section through the ECAP die a) with $\Psi = 0$ and b) $\Psi \neq 0$ [8].

The specimen pressed through the ECAP die is deformed by a simple shear in the intersection point of the channels. The imposed strain in each ECAP pass is dependent primarily upon the angle *Φ* and, to a lesser extent, on the angle *Ψ*. It can be shown from the first principles that the imposed strain ε_N after N passes is given by a relation in the form [8]:

$$\epsilon_N = \frac{N}{\sqrt{3}}\left[2cotg\left(\frac{\Phi}{2}+\frac{\Psi}{2}\right)+\Psi cosec\left(\frac{\Phi}{2}+\frac{\Psi}{2}\right)\right]. \qquad (1)$$

2.2. High-pressure torsion

High-pressure torsion (HPT) is another well-known SPD technique. In this method, the mechanical properties of a material are improved by a high pressure and concurrent torsional straining [9]. HPT was also for the first time applied to metals in the former Soviet Union in the 1980s [10]. The experimental setup of HPT is schematically illustrated in Figure 2.

The typical size of the disk-shaped sample varies from 10 to 20 mm in diameter and about 1 mm in thickness. A disk sample is placed between two anvils where it is subjected to a compressive pressure of several GPa. Simultaneously, one of the anvils rotates and the torsional strain is imposed to the sample.

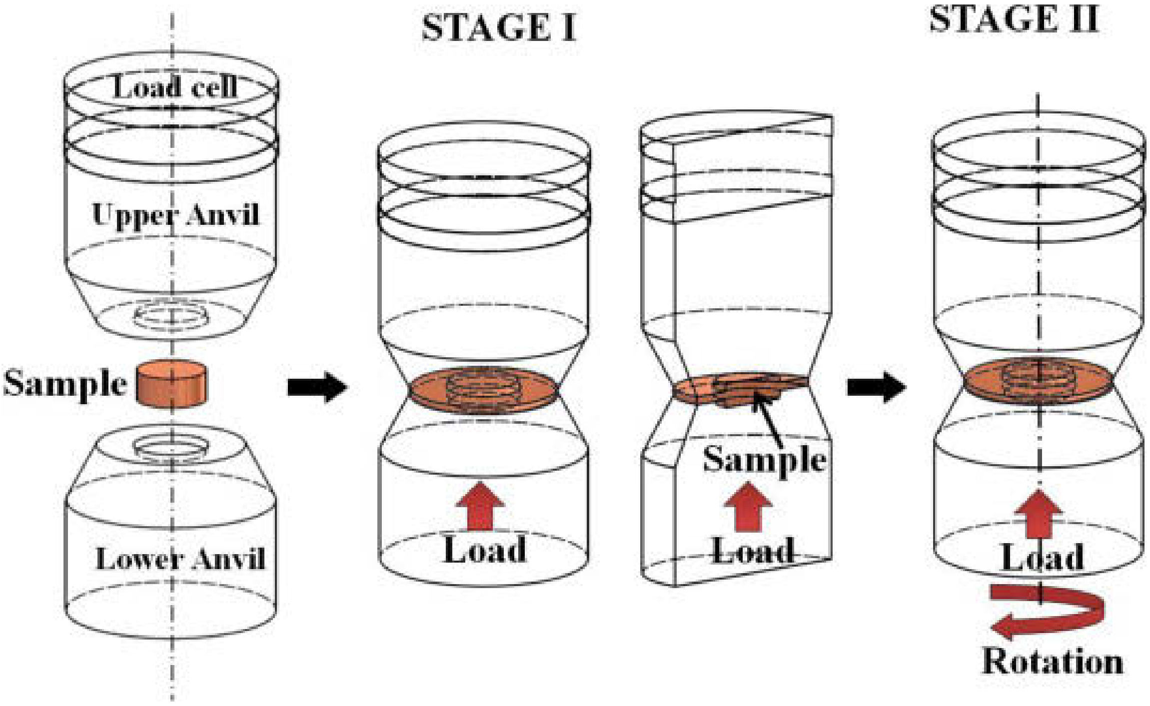

Figure 2. Schematic of the HPT device showing the set-up, compression stage (stage I), and compression-torsion stage (stage II) [11].

The total strain imposed by HPT in the sample can be calculated by different approaches. The first widely used approach (Hencky/Eichinger) can be expressed by the logarithmic relation [12]:

$$\epsilon = ln\left(\frac{2\pi N r h_0}{h^2}\right), \tag{2}$$

where N is the number of rotations, r represents the radius of the sample, and h_0 and h its initial and final thickness, respectively. The second possible approach (von Mises) using a model of simple torsion could be expressed by the following linear relation [13]:

$$\epsilon = \frac{\gamma}{\sqrt{3}} = \frac{r\theta}{\sqrt{3}h} = \frac{2\pi N r}{\sqrt{3}h}, \tag{3}$$

where γ is the shear strain and θ is the rotation angle.

However, the real strain generated in the workpiece during HPT may be different depending mainly on the die geometry and other factors. No unambiguous conclusion was adopted whether the Hencky or von Mises strain describes better the total strain imposed by HPT. Finite element method (FEM) may be employed to analyze the plastic deformation distribution in specimens processed by HPT. Several authors [14, 15] have used the FEM technique to determine the stress distribution and other parameters, e.g., the influence of the coefficient of friction, torque, etc. Recently, Lee et al. [13] employed a combined analysis of FEM and the model of dislocation cell evolution to describe the local deformation in specimen processed by HPT. The results of this study are shown in Figure 3.

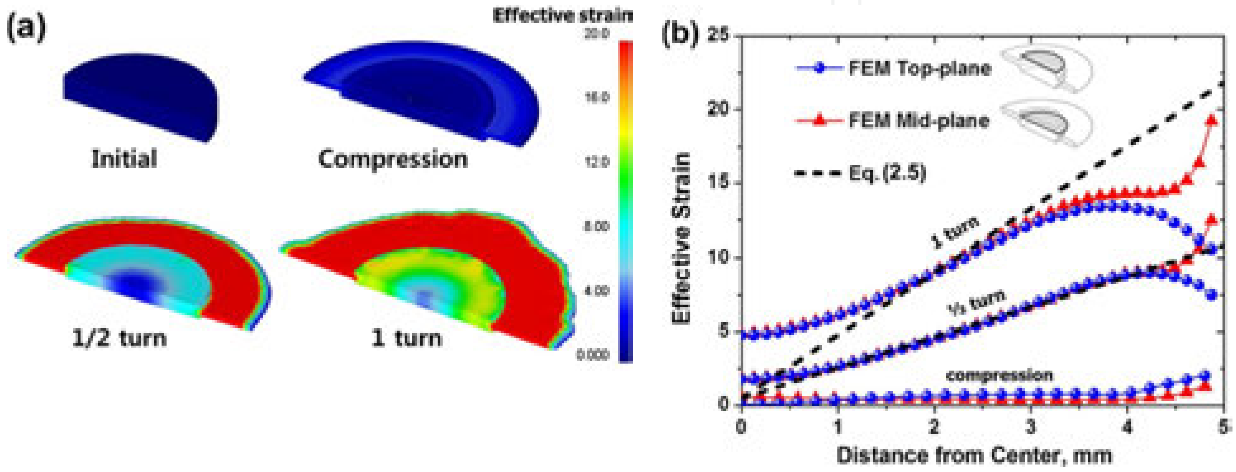

Figure 3. FEM simulation of effective strain imposed by HPT. a) The effective strain distribution of the as compressed specimen (N=0), the specimens after 1/2 (N=1/2) and 1 turn (N=1). b) The effective strain distribution throughout the thickness of the specimens N=0, N=1/2, and N=1 in the top and mid-plane showing the comparison of the FEM simulations [13] with the theoretical strain (Eq. 2.5).

Figure 3: FEM simulation of effective strain imposed by HPT. a) The effective strain distribution of the as compressed specimen (N=0), the specimens after 1/2 (N=1/2) and 1 turn (N=1). b) The effective strain distribution throughout the thickness of the specimens N=0, N=1/2, and N=1 in the top and mid-plane showing the comparison of the FEM simulations [13] with the theoretical strain (Eq. 2.5).

2.3. Material processing

2.3 Material processing

Prior to ECAP, the material was extruded at 350°C with an extrusion ratio of 22. ECAP pressing was performed at 180°C following route B_C, i.e., rotating the sample 90° between the individual passes, with the velocity of 50 mm/min. The angle Φ between two intersecting channels and the corner angle Ψ were 90° and 0°, respectively. Both channels have a square cross section of 10 mm × 10 mm. A series of specimens after N = 1, 2, 4, 8, and 12 passes was processed by ECAP. The as-extruded specimen was also included in the investigation as the reference material (marked N = 0).

Prior to HPT, the material was homogenized at 390°C for 12 hours. After homogenization, the disk specimens of the diameter of 19 mm and the thickness of 1-2 mm were cut from the billet. These specimens were processed by quasi-constrained HPT at room temperature for N = ¼, ½, 1, 5, and 15 rotations. In addition to samples subjected to various number N of HPT rotations, a sample that was pressed only between the anvils but not subjected to any HPT rotation (N = 0) was investigated as well.

Prior to ECAP, the material was extruded at 350°C with an extrusion ratio of 22. ECAP pressing was performed at 180°C following route B_C, i.e., rotating the sample 90° between the individual passes, with the velocity of 50 mm/min. The angle Φ between two intersecting channels and the corner angle Ψ were 90° and 0°, respectively. Both channels have a square cross section of 10 mm ×10 mm. A series of specimens after N = 1, 2, 4, 8, and 12 passes was processed by ECAP. The as-extruded specimen was also included in the investigation as the reference material (marked N = 0).

Prior to HPT, the material was homogenized at 390°C for 12 hours. After homogenization the disk specimens of the diameter of 19 mm and the thickness of 1-2 mm were cut from the billet. These specimens were processed by quasi-constrained HPT at room temperature for N = ¼, ½, 1, 5, and 15 rotations. In addition to samples subjected to various number N of HPT rotations, a sample that was pressed only between the anvils but not subjected to any HPT rotation (N = 0) was investigated as well.

2.4 Experimental techniques of microstructure investigation

2.4.1 Light microscopy

The specimen surface for light microscopy observation needs to be plain, without impurities or scratches. Polypropylene was used for mounting the specimens for better manipulation. Mounted specimens were prepared by three consequent procedures: mechanical grinding, polishing, and etching. In the first step, the specimens were mechanically grinded on watered abrasive papers. Then the specimens were polished on a polishing disc with polishing suspension of grade 3 and 1 µm. Using this procedure, flat specimens with minimum surface scratches were obtained. Finally, the polished samples were etched by a diluted solution of picric acid. The time period of etching has to be optimized to attain the best possible

2.4. Experimental techniques of microstructure investigation

2.4.1. Light microscopy

The specimen surface for light microscopy observation needs to be plain, without impurities or scratches. Polypropylene was used for mounting the specimens for better manipulation. Mounted specimens were prepared by three consequent procedures: mechanical grinding, polishing, and etching. In the first step, the specimens were mechanically grinded on watered abrasive papers. Then the specimens were polished on a polishing disc with polishing suspension of grade 3 and 1 μm. Using this procedure, flat specimens with minimum surface scratches were obtained. Finally, the polished samples were etched by a diluted solution of picric acid. The time period of etching has to be optimized to attain the best possible visibility and no artefacts on the surface [16].

2.4.2. Electron Backscatter Diffraction (EBSD)

Electron backscatter diffraction (EBSD) is a microstructural crystallographic technique for determining crystallographic orientation. Texture, grain size and distribution, the misorientation and shape of individual grains, the types of grain boundaries, and many other microstructural features may be obtained from EBSD results.

The principle of the EBSD method is that the accelerated high-energy electrons interact with the atomic lattice of the crystalline material and form the so-called Kikuchi lines on the screen. The measurement is done automatically with a defined step. The formation of Kikuchi lines is caused by inelastic electron scattering. The inelastically scattered electron wavelength is slightly higher than the wavelength of elastically scattered electrons and the inelastic scattered electron intensity decreases with increasing scattering angle. In certain crystal orientations, some planes satisfy the Bragg condition (with diffraction angle θ), and the inelastically scattered electrons are Bragg diffracted. These electrons are called Kikuchi electrons. Kikuchi electrons move along conical surfaces whose top angle is equal ($\pi - 2\theta$) and the axis of diffraction planes is the normal line. Two hyperbolas are formed by the intersection of the conical surfaces and a screen. The hyperbolas seem like straight lines in the central part of the electron diffractogram and the distance between lines corresponds to the angle 2θ [16].

The SEM FEI Quanta 200 FX equipped with EDAX EBSD camera and OIM software was utilized for EBSD observations. A field emission gun (FEG) of a Schottky type was used as a source of electrons in the microscope. Beam voltage in the range from 500 V to 30 kV is applicable. The acceleration voltage employed was 10 kV.

The samples for EBSD investigation were first mechanically grinded on watered abrasive papers of grade 800, 1200, 2400, and 4000, respectively. Then the specimens were mechanically polished with diamond suspensions for water-sensitive materials of grade 3, 1, and ¼ μm, respectively. The final ion-polishing using a Gatan PIPS device was used to remove the surface layer influenced by polishing.

2.4.3. Transmission Electron Microscopy (TEM)

Transmission electron microscopy (TEM) is a technique that studies the local microstructure of the material using a beam of high-energy electrons. The specimens for TEM have to be very thin (≈ 100 nm depending on the acceleration voltage). An image is formed from the interaction of the electrons transmitted through the specimen and focused on a fluorescent screen or CCD camera.

The sample (thin foil) preparation consists of two steps: mechanical thinning and polishing. The type of polishing depends on the physical and chemical properties of the material.

The specimens of AZ31 alloy were first cut from the billet plane X (perpendicular to the extrusion direction) into slices of the thickness of approximately 1 mm. The slices were mechanically grinded from both sides to the thickness of 100 μm. The 3 mm diameter disks were cut out of the thin slices and dimpled from one side to the thickness of approximately 30 μm using the Gatan dimple grinder. This dimpling technique reduces electrolytic or ion polishing times and ensures that the ultra-thin area is done in the central part of the foil.

Ion polishing is used for materials that cannot be polished electrolytically. It is the case of many Mg alloys including AZ31. Ion polishing is a method of removing very fine quantities of the material. It uses an inert gas (argon) to generate a plasma stream that is emitted to the thinned area of the sample and removes the individual layers of the material. Acceleration energies vary usually from 2 to 4 keV. Ion beam always enters the sample. The penetration depth depends on the angle between the direction of the ion beam and the sample surface. The optimum conditions found for AZ31 were the following: acceleration voltage of 4 kV, angle of incidence of 4°, and room temperature. In the final stage the acceleration, voltage was reduced to 2 kV and the angle of incidence to 2°. The specimen preparation for TEM is finished when a small hole is formed in the foil and the surrounding area is thin enough to allow high-energy electrons to pass through the specimen. The schematic of the Precision Ion-Polishing System (PIPS) used for ion polishing is displayed in Figure 4 [17].

The microstructure observations were made with the TEM JEOL 2000FX at Charles University in Prague. The applied accelerated voltage was 200 kV.

2.4.4. Automated Crystallographic Orientation Mapping in a TEM (ACOM-TEM)

Automated crystallographic orientation mapping in a TEM (ACOM-TEM) is an effective technique for mapping phase and crystal orientation and an alternative to the well-known EBSD attachment SEM based on the Kikuchi lines. ACOM-TEM was first introduced by Schwarzer et al. [18]. This method of microstructural characterization represents a powerful tool especially for UFG or nano-grained materials where the limited resolution of SEM disallows EBSD scans. Its basic principle is similar to EBDS mapping—a selected area is scanned with defined step size and the electron diffraction patterns are collected using an external CCD camera. Off-line, every diffraction pattern is compared to the pre-calculated template and the best match is selected. The main difference with respect to EBSD is that point diffraction patterns are analyzed instead of Kikuchi lines, which significantly increases the

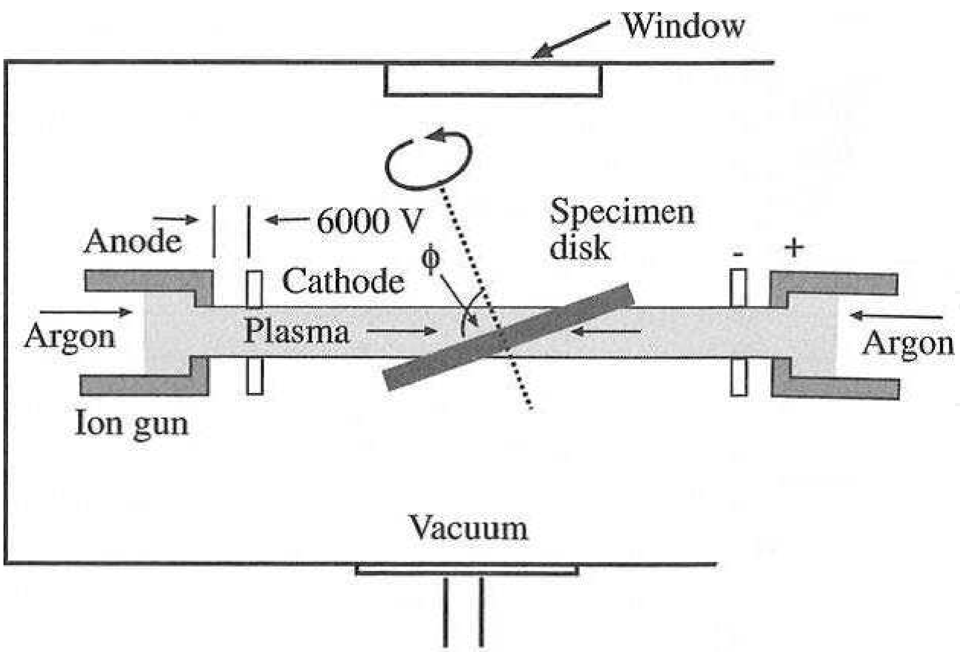

Figure 4. Schematic illustration of Precision Ion-Polishing System (PIPS).

precision of orientation determination. This type of ACOM-TEM device was developed in Grenoble by E. Rauch et al. [19, 20].

The experimental measurements were carried out using a TEM Philips CM200 equipped with a LaB_6 gun at 200 kV at Université Libre de Bruxelles in Belgium. For the data treatment, TSL OIM Analysis 5 was used.

3. Results and discussion

3.1. Microstructure evolution of AZ31 processed by ECAP

3.1.1. Light microscopy

The limited resolution of light microscopy allows to perform only overview images with no structure details. Typical examples of microstructure evolution of extruded specimen and the specimens processed by different number of ECAP passes (N) are shown in Figure 5. The extruded sample microstructure shown in Figure 5a consists of two types of grains—several large grains surrounded by many small grains. The microstructure developed only slightly after the first and the second ECAP pass, the bimodal structure is still observed (see Figure 5b). The microstructure changes begin to be significant in light microscopy after 4 ECAP passes. One can see in Figure 5c that the large grains become smaller. However, the bimodal structure is not observed after 8 and 12 ECAP passes. The homogeneous microstructure of sample after 12 ECAP passes is shown in Figure 5d.

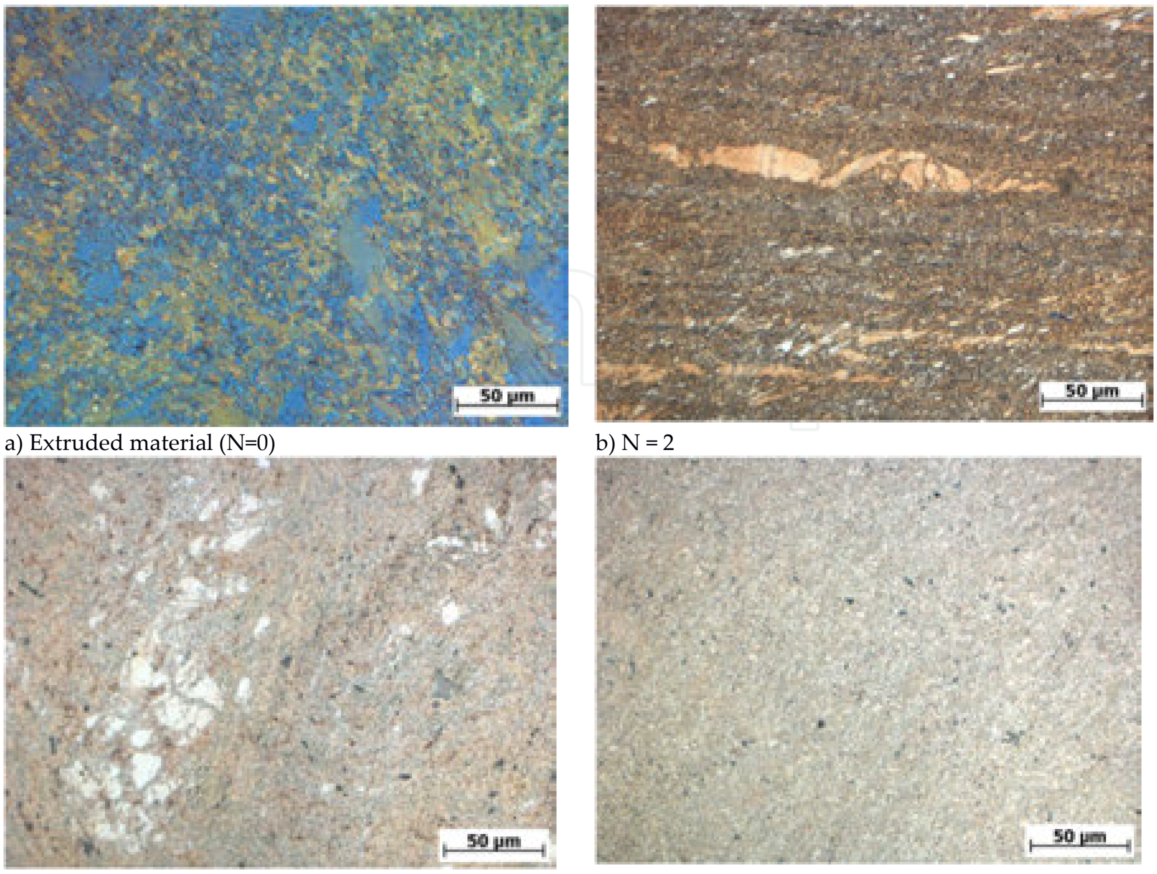

a) Extruded material (N=0) b) N = 2

c) N = 4 d) N = 12

Figure 5: The microstructure of the extruded and ECAPed AZ31 alloy.

Figure 5. The microstructure of the extruded and ECAPed AZ31 alloy.

3.1.2 EBSD

3.1.2. EBSD

Figure 6 shows the microstructure and texture of the extruded AZ31 alloy. The EBSD inverse pole figure map is in the extrusion direction (ED). The microstructure of the initial extruded bar (0P) consists of large grains of 50–100 ≈m mixed with relatively fine grains of 2–5 µm. Most grains have their crystallographic c-axis perpendicular to the extrusion direction (ED), i.e., <10.0> axes parallel to the ED, which is typically found after extrusion of Mg alloys [21].

Figure 6 shows the microstructure and texture of the extruded AZ31 alloy. The EBSD inverse pole figure map is in the extrusion direction (ED). The microstructure of the initial extruded bar (0P) consists of large grains of 50–100 ≈m mixed with relatively fine grains of 2–5 μm. Most grains have their crystallographic c-axis perpendicular to the extrusion direction (ED), i.e., <10.0> axes parallel to the ED, which is typically found after extrusion of Mg alloys [21].

Figure 7 presents the microstructure and texture of the sample after 1 ECAP pass (1P). EBSD measurements were carried out at the mid-part of the cross-section of the billet. Sample coordinate system, i.e., X–Y–Z directions, which is used for representing the texture are illustrated in Figure 7d.

As shown in Figure 7a, the bimodal distribution of grain sizes is still observed in the 1P sample. A new texture component that corresponds to the basal poles rotated about 40° from the initial orientation towards the pressing direction is visible in the 1P sample, Figure 7b. The mentioned orientation change, however, is observed mainly in large grains (grain size> 10 μm). Figure 7c presents the (0001) pole figure of grains smaller than 3 μm in the 1P sample. The intensity of the tilted basal poles is rather weak compared to the pole figure constructed using all grains.

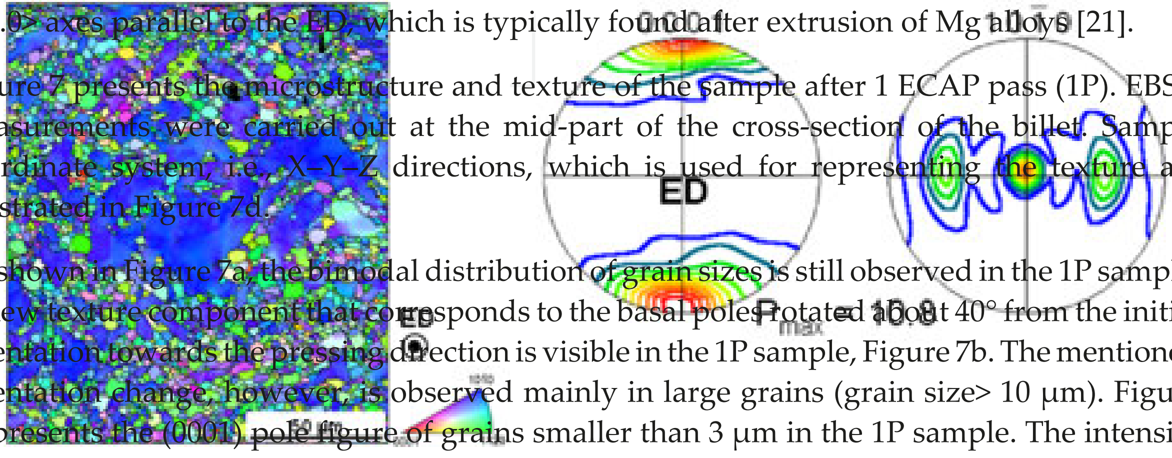

(a) (b)

Figure 6: (a) EBSD orientation map and (b) recalculated pole figures of the extruded bar (0P), measured at the cross-section transverse to the extrusion direction (contour level = 1, 2, ...10).

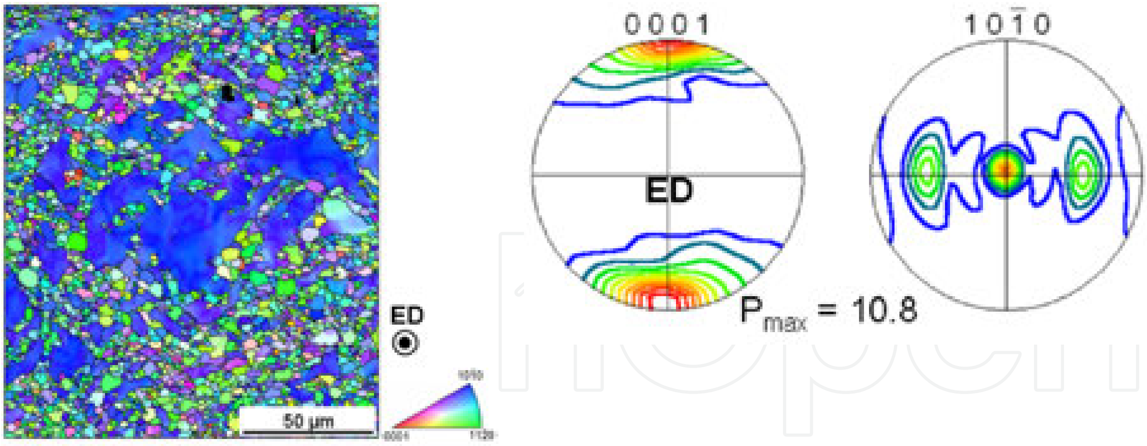

(a) (b)

Figure 6: (a) EBSD orientation map and (b) recalculated pole figures of the extruded bar (0P), measured at the cross-section transverse to the extrusion direction (contour level = 1, 2, …10).

Figure 6. (a) EBSD orientation map and (b) recalculated pole figures of the extruded bar (0P), measured at the cross-section transverse to the extrusion direction (contour level = 1, 2,...10).

Figure 7 presents the microstructure and texture of the sample after 1 ECAP pass (1P). EBSD measurements were carried out at the mid-part of the cross-section of the billet. Sample coordinate system, i.e., X-Y-Z directions, which is used for representing the texture are illustrated in Figure 7d.

As shown in Figure 7a, the bimodal distribution of grain sizes is still observed in the 1P sample. A new texture component that corresponds to the basal poles rotated about 40° from the initial orientation towards the pressing direction is visible in the 1P sample, Figure 7b. The mentioned orientation change, however, is observed mainly in large grains (grain size> 10 µm). Figure 7c presents the (0001) pole figure of grains smaller than 3 µm in the 1P sample. The intensity of the tilted basal poles is rather weak compared to the pole figure constructed using all grains. Moreover, the small grains (< 3 µm) with the tilted basal pole are found mainly in neighboring areas around large grains.

These results regarding distinct textures depending on the grain sizes indicate that the shear strain by the first ECAP pass is mainly accommodated within the large grains in accordance with the Hall–Petch relation. The discontinuity of material flow caused by the inhomogeneous deformation seems to be compensated by the occurrence of the dynamic recrystallization in the vicinity of grain boundaries of large grains, such that the sample could be deformed without failure.

Moreover, the small grains (< 3 µm) with the tilted basal pole are found mainly in neighboring areas around large grains.

These results regarding distinct textures depending on the grain sizes indicate that the shear strain by the first ECAP pass is mainly accommodated within the large grains in accordance with the Hall–Petch relation. The discontinuity of material flow caused by the inhomogeneous deformation seems to be compensated by the occurrence of the dynamic recrystallization in the vicinity of grain boundaries of large grains, such that the sample could be deformed without failure.

Microstructural features of the sample after 2 ECAP passes (not shown here) are very similar to those after 1 ECAP pass, i.e., the bimodal distribution of grain sizes and the orientation change in large grains remain almost unchanged.

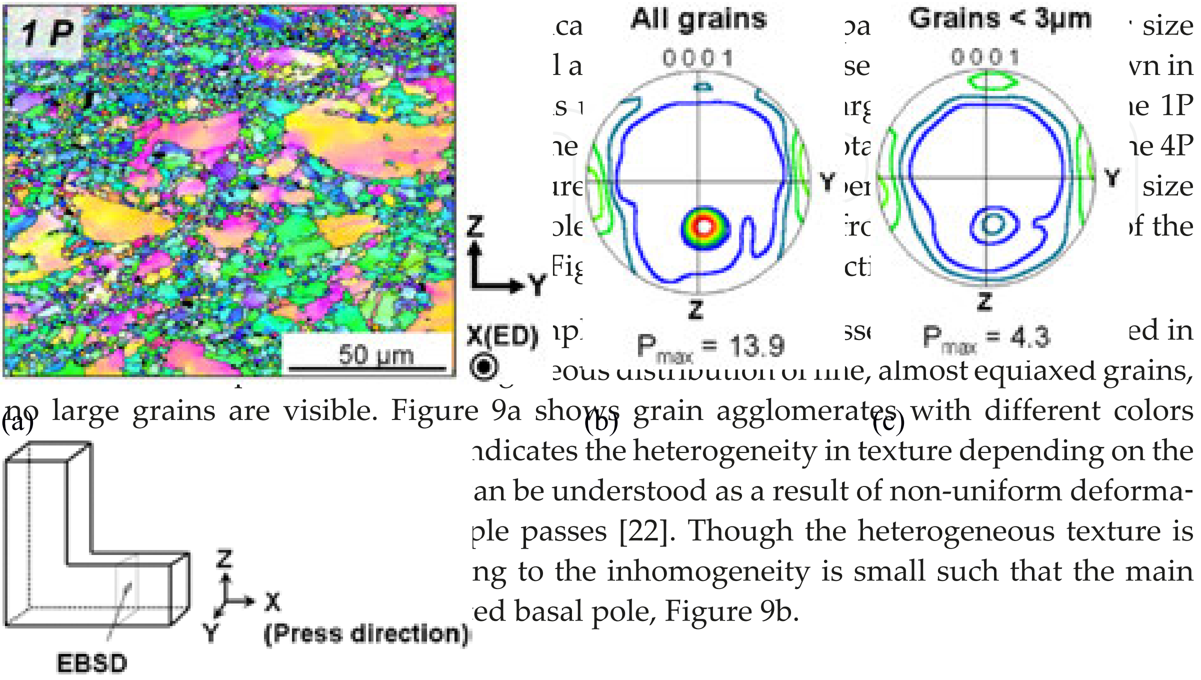

The ca pa size becc l a se vn in Figu s rg ne 1P sam ne ota ne 4P sam ure per size disa ole rc f the EBS Fig cti

The p. ss ed in Figu eous distribution of fine, almost equiaxed grains, i.e., no large grains are visible. Figure 9a shows grain agglomerates with different colors dist ndicates the heterogeneity in texture depending on the loca an be understood as a result of non-uniform deformation ple passes [22]. Though the heterogeneous texture is visi ng to the inhomogeneity is small such that the main text ed basal pole, Figure 9b.

to the pole figure constructed using all grains. Moreover, the small grains (< 3 μm) with the tilted basal pole are found mainly in neighboring areas around large grains.

These results regarding distinct textures depending on the grain sizes indicate that the shear strain by the first ECAP pass is mainly accommodated within the large grains in accordance with the Hall–Petch relation. The discontinuity of material flow caused by the inhomogeneous deformation seems to be compensated by the occurrence of the dynamic recrystallization in the vicinity of grain boundaries of large grains, such that the sample could be deformed without failure.

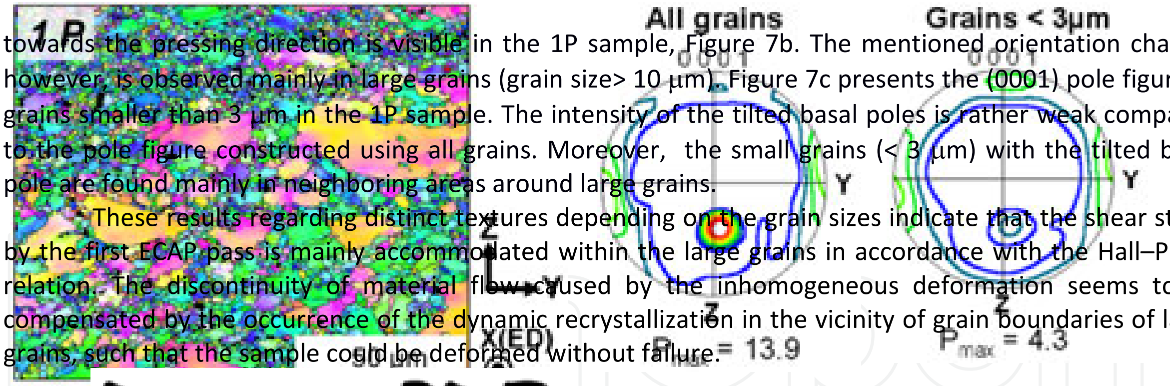

towards the pressing direction is visible in the 1P sample, Figure 7b. The mentioned orientation change, however, is observed mainly in large grains (grain size> 10 μm). Figure 7c presents the (0001) pole figure of grains smaller than 3 μm in the 1P sample. The intensity of the tilted basal poles is rather weak compared

to the pole figure constructed using all grains. Moreover, the small grains (< 3 μm) with the tilted basal pole are found mainly in neighboring areas around large grains.

These results regarding distinct textures depending on the grain sizes indicate that the shear strain by the first ECAP pass is mainly accommodated within the large grains in accordance with the Hall–Petch relation. The discontinuity of material flow caused by the inhomogeneous deformation seems to be compensated by the occurrence of the dynamic recrystallization in the vicinity of grain boundaries of large grains, such that the sample could be deformed without failure.

(a) (b) (c)

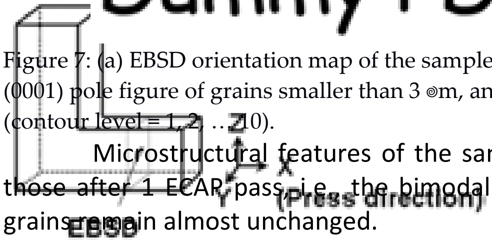

(d)

Figure 7: (a) EBSD orientation map of the sample after 1 ECAP pass, (b) (0001) pole figure calculated using all grains, (c) (0001) pole figure of grains smaller than 3 ⊚m, and (d) the scheme of the geometry of specimens for EBSD measurements (contour level = 1, 2, … 10).

Microstructural features of the sample after 2 ECAP passes (not shown here) are very similar to those after 1 ECAP pass, i.e., the bimodal distribution of grain sizes and the orientation change in large grains remain almost unchanged.

The amount of large grains decreases significantly after 4 ECAP passes (4P), and their size becomes smaller when compared to the initial and the 1P samples (see Figure 8). As shown in Figure 8a with dashed circles, the fine grains usually surround large grains. Unlike the 1P sample, the fine grains (<3 μm) have mainly the orientation of the rotated basal poles in the 4P sample (Figure 8c). It is clear that the texture heterogeneity depending on the grain size disappears after 4 ECAP passes, compared pole figures evaluated from the whole area of the EBSD measurement to that from fine grains, Figure 8b and c, respectively.

Figure 7: (a) EBSD orientation map of the sample after 1 ECAP pass, (b) (0001) pole figure calculated using all grains, (c) (0001) pole figure of grains smaller than 3 ⊚m, and (d) the scheme of the geometry of specimen for EBSD measurements (contour level = 1, 2, … 10).

Figure 7. (a) EBSD orientation map of the sample after 1 ECAP pass, (b) (0001) pole figure calculated using all grains, (c) (0001) pole figure of grains smaller than 3 μm, and (d) the scheme of the geometry of specimens for EBSD measurements (contour level = 1, 2, … 10).

Microstructural features of the sample after 2 ECAP passes (not shown here) are very similar to those after 1 ECAP pass, i.e., the bimodal distribution of grain sizes and the orientation change in large

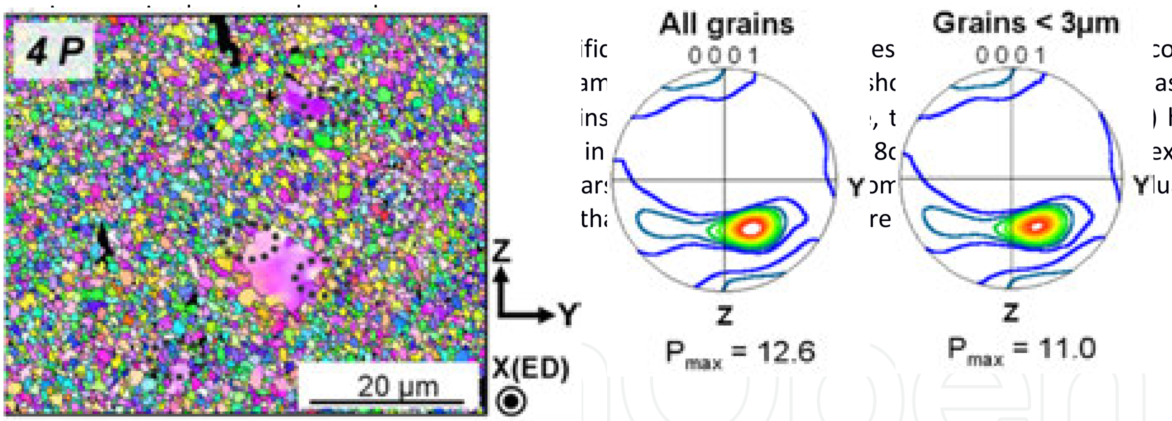

(a) (b) (c)

Figure 8: (a) EBSD orientation map of the sample after 4 ECAP passes, (b)(0001) pole figure of all grains, and (c) grains smaller than 3 ⊚m (contour level = 1, 2, … 10).

Figure 8. (a) EBSD orientation map of the sample after 4 ECAP passes, (b)(0001) pole figure of all grains, and (c) grains smaller than 3 μm (contour level = 1, 2,… 10).

The microstructure and the texture of the sample after 12 ECAP passes (12P) are presented in Figure 9. The 12P sample shows the homogeneous distribution of fine, almost equiaxed grains, i.e., no large grains are visible. Figure 9a shows grain agglomerates with different colors distributed along a diagonal line. This indicates the heterogeneity in texture depending on the locations. This texture inhomogeneity can be understood as a result of non-uniform deformation along the ECAP billet after multiple passes [22]. Though the heterogeneous texture is visible, the fraction of the grains relating to the inhomogeneity is small such that the main texture component is found at the rotated basal pole, Figure 9b.

Figure 10 displays size distributions of fine grains (< 10 μm) after different numbers of ECAP passes. This variation in the area fraction of large grains (>10 μm) is shown in Table 1. Grains smaller than 3 μm present in the extruded sample (0P) become finer (μ 1 Im) after the first ECAP pass. In subsequent ECAP passes no significant change in the size distribution in the range of the relatively fine grains is observed, while the area fraction of grains larger than 10 ≈m decreases gradually with ECAP passes, see Table 1.

The microstructure and the texture of the sample after 12 ECAP passes (12P) are presented in Figure 9. The 12P sample shows the homogeneous distribution of fine, almost equiaxed grains, i.e., no large grains are visible. Figure 9a shows grain agglomerates with different colors distributed along a diagonal line. This indicates the heterogeneity in texture depending on the locations. This texture inhomogeneity can be understood as a result of non-uniform deformation along the ECAP billet after multiple passes [22]. Though the heterogeneous texture is visible, the fraction of the grains relating to the inhomogeneity is small such that the main texture component is found at the rotated basal pole, Figure 9b.

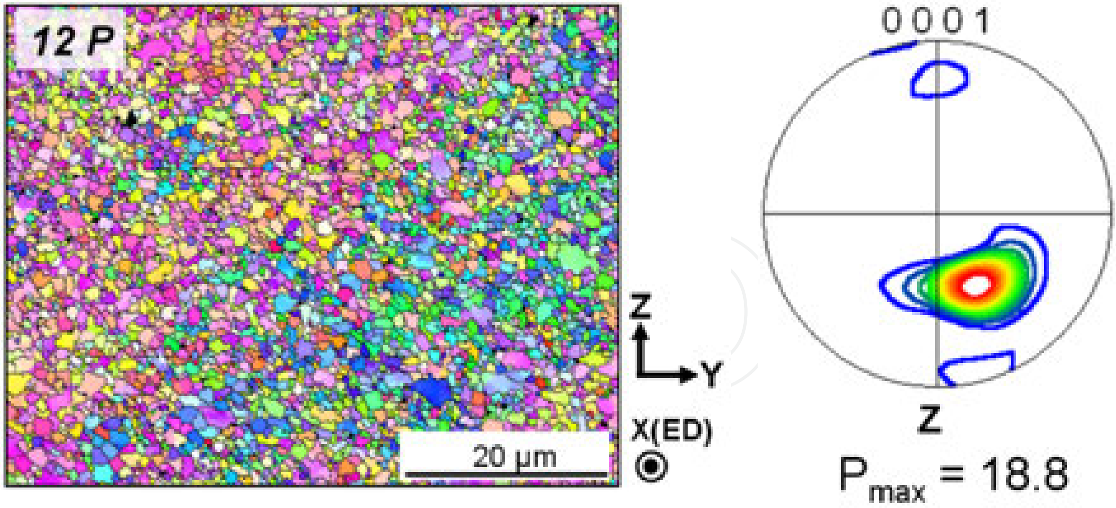

(a) (b)

Figure 9: (a) EBSD orientation map and (b) (0001) pole figure of the sample after 12 ECAP passes (contour level =

Figure 9. (a) EBSD orientation map and (b) (0001) pole figure of the sample after 12 ECAP passes (contour level = 1, 2,… 15).

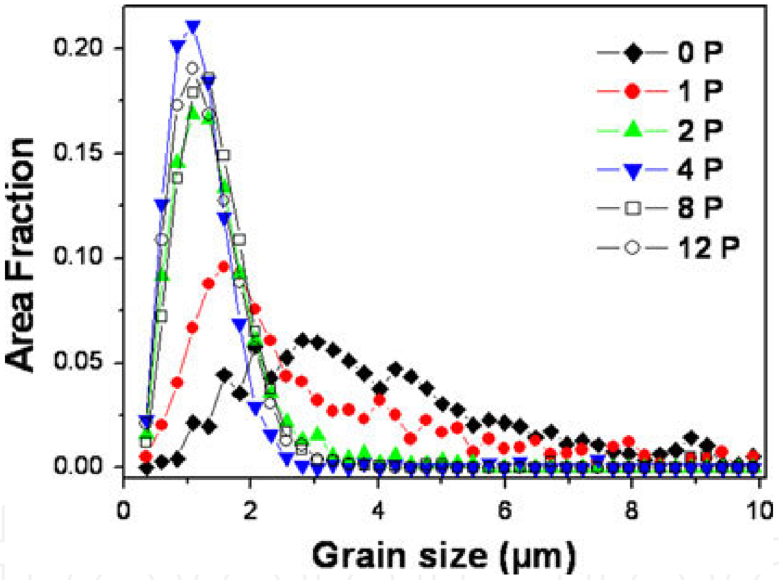

Figure 10. Grain size distributions within the range up to 10 μm and the area fraction of the grains larger than 10 μm as a function of the ECAP pass number.

No. ECAP Passes	0	1	2	4	8
Area fraction of grains > 10μm	17.9%	18.1%	7.9%	2.8%	None

Table 1. Area fraction of large grains as a function of ECAP pass number.

The variation in the fraction of low-angle boundaries (misorientation angle < 15°, LAGB) and high-angle boundaries (misorientation angle > 15°, HAGB) as a function of the ECAP pass number is shown in Figure 11. The LAGB fraction increases after 1 ECAP pass to µ 50%, and is significantly reduced (≈20%) after two ECAP passes and remains almost unchanged as the number of passes increases above 2. This stabilization of the HAGB formed by 2 ECAP passes indicates that the dislocations generated by ECAP did not reach the level necessary for the formation of dislocation in the cell-structure and further development of HAGB. Since the ECAP in this study was carried out at moderate temperature, the dislocation annihilation process by dynamic recovery occurred fast enough such that the grains could not be further refined after 2 ECAP passes.

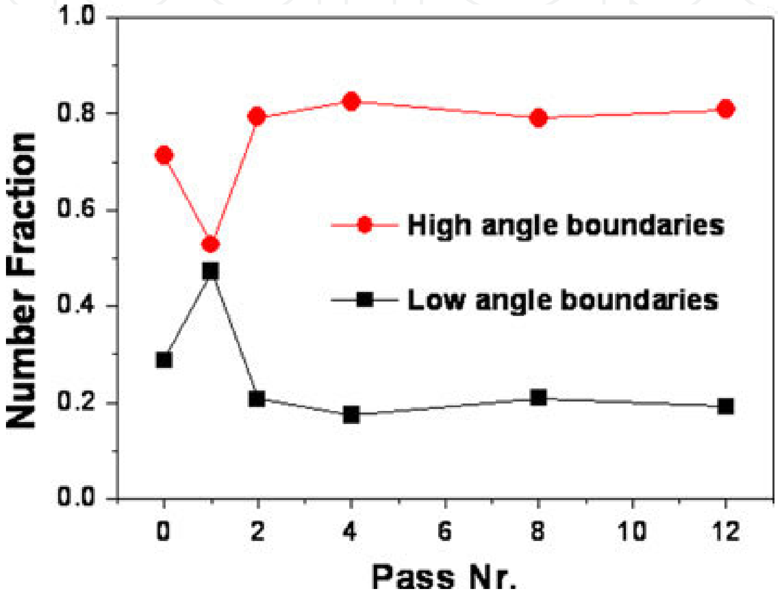

Figure 11. Variation of fraction of the HAGB and LAGB as functions of the ECAP pass number.

3.1.3. TEM

Additional detailed observations using TEM broadened the EBSD research. The samples for TEM observations were cut perpendicular to the pressing direction from the EX-ECAPed billet and prepared by mechanical grinding, dimpling, and ion polishing. The microstructure of extruded samples is bimodal—consists of large grains of 50–100 µm mixed with relatively fine grains of 2–5 µm. Figure 12 shows the area with smaller grains of the average size of few µm. Typical twins are clearly seen in several grains. The (0001) basal texture of individual grains in extruded magnesium alloy observed in EBSD measurements was confirmed by electron diffraction analysis. The contrast of individual grains on this micrograph with typical low-angle grain boundaries confirmed the analysis of diffraction patterns. The area of larger grains had a typical heavily deformed structure with high density of tangled dislocations (not shown here).

Figure 13 presents the microstructure of the specimen after 1 EX-ECAP pass. The bimodal character of the microstructure did not change after the first ECAP pass; the average grain size is only slightly smaller in comparison with the extruded material, see Figure 13a. However,

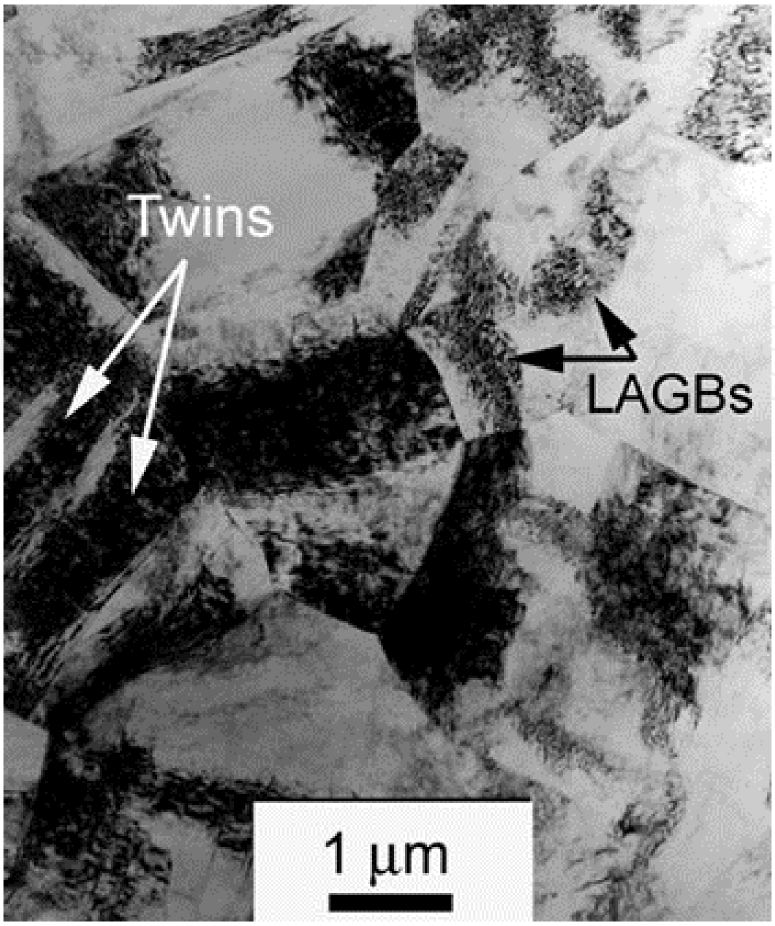

Figure 12. Transmission electron micrograph of extruded AZ31 alloy.

one significant difference between these two micrographs is observed, namely the character of grain boundaries. One can see many high-angle grain boundaries with typical thickness fringe band contrast confirming their almost equilibrium state in this micrograph. On the other hand, several grain boundaries remained in a non-equilibrium state with diffuse fuzzy contrast and many dislocations lying in a grain boundary plane were also observed. Several areas with high density of tangled dislocations with no or only exceptional signs of substructure formation were found in this specimen, see Figure 13b.

Subsequent TEM observation confirmed that the microstructure of EX-ECAPed samples changed only partly with increasing number of ECAP passes—fine grains were refined only slightly while the large grain zones were refined significantly. Typical microstructure of the sample processed by 2 EX-ECAP passes is shown in Figure 14.

Only fine grains of the average grain size in the submicrometer range were observed in the micrographs of the specimens after 8 and 12 ECAP passes. Figure 15a presents the typical microstructure of the sample after 8 passes. One can see that the grains in this micrograph are equiaxed, and the grain size is approximately 800 nm. This material has significantly lower density of dislocations and equilibrium grains boundaries. A few newly recrystallized very small grains with no dislocations and sharp equilibrium boundaries were also found in the

see many high-angle grain boundaries with typical thickness fringe band contrast confirming
equilibrium state in this micrograph. On the other hand, several grain boundaries remain
equilibrium state with diffuse fuzzy contrast and many dislocations lying in a grain boundary
also observed. Several areas with high density of tangled dislocations with no or only excepti
substructure formation were found in this specimen, see Figure 13b.

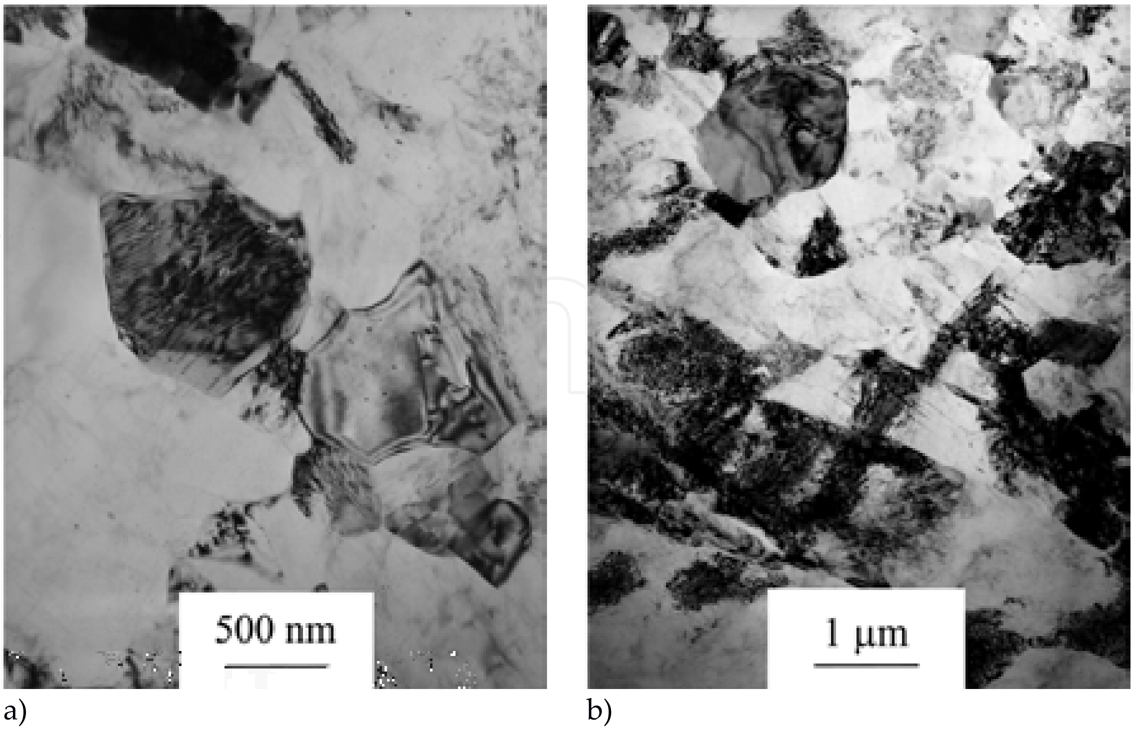

a) b)

Figure 13: Transmission electron micrographs of AZ31 alloy after extrusion and 1 pass of ECA
equilibrium and HAGB region and (b) nonequilibrium GB region.

Figure 13. Transmission electron micrographs of AZ31 alloy after extrusion and 1 pass of ECAP, (a) equilibrium and HAGB region and (b) nonequilibrium GB region.

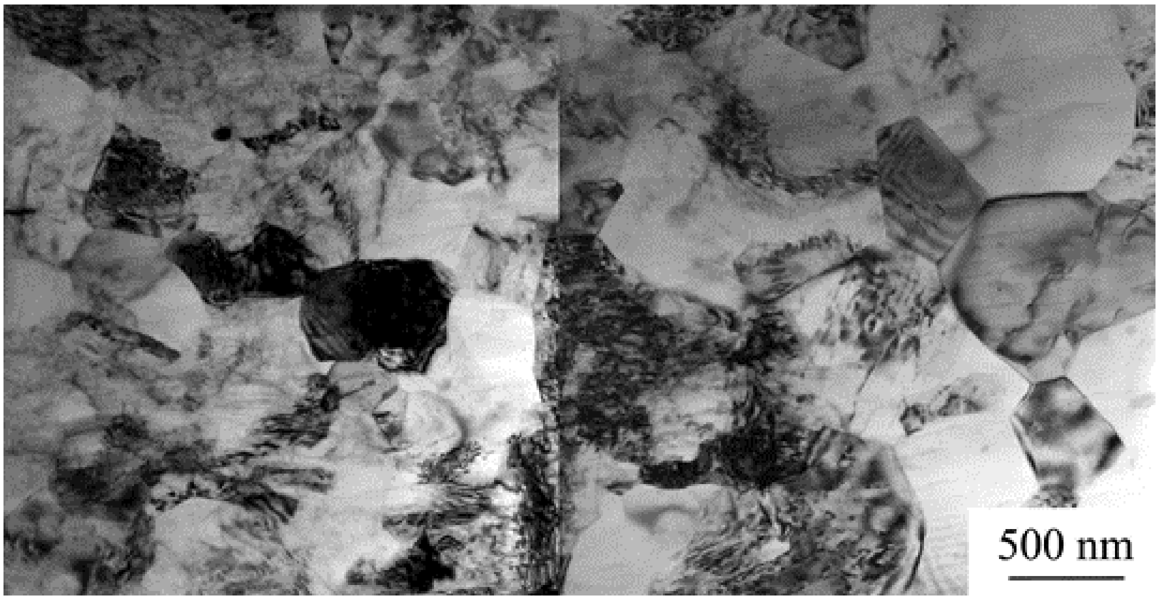

Figure 14. Transmission electron micrograph of AZ31 alloy after extrusion and 2 passes of ECAP.

microstructure after 8 and 12 passes of ECAP as seen in Figure 15b. TEM observations confirm the process of microstructure evolution and its fragmentation as observed by EBSD. In particular, large grains were continuously refined during subsequent ECAP pressing while the fine grains remained almost unchanged.

boundaries were also found in the microstructure after 8 and 12 passes of ECAP as seen in Figure 15b. TE observations confirm the process of microstructure evolution and its fragmentation as observed by EBS In particular, large grains were continuously refined during subsequent ECAP pressing while the fine grai remained almost unchanged.

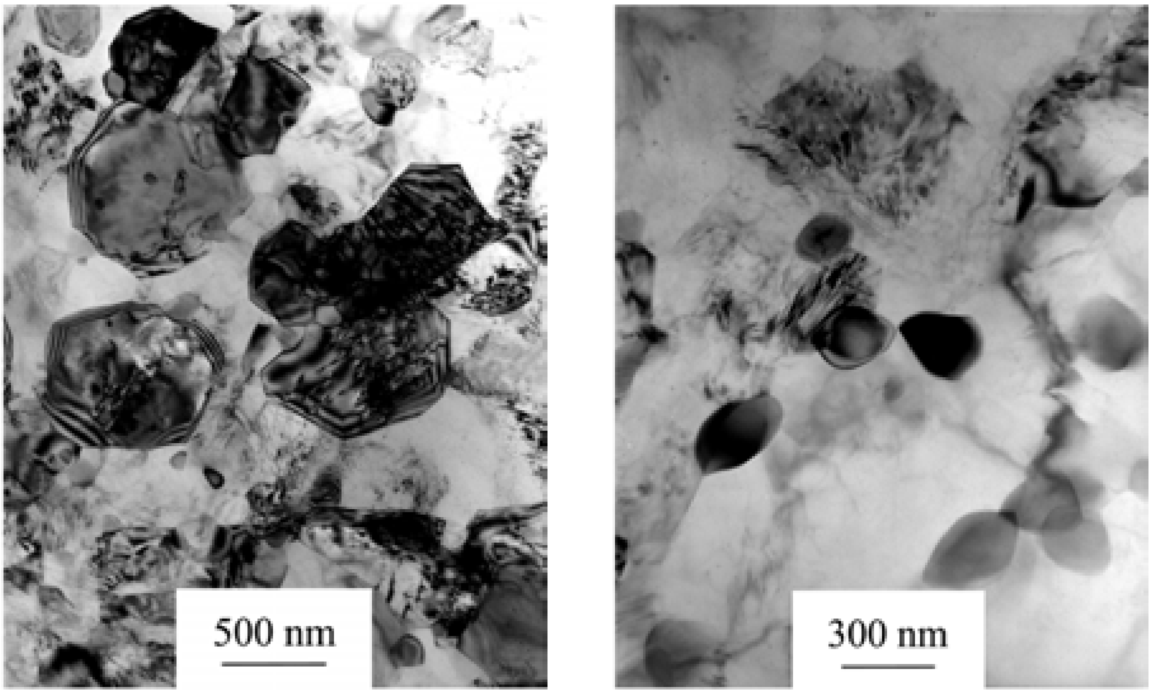

a) b)

Figure 15. Transmission electron micrograph of the AZ31 alloy (a) after 8 passes of EX-ECAP and (b) newly recrystallized small grains after 12 passes of EX-ECAP.

Figure 15. Transmission electron micrograph of the AZ31 alloy (a) after 8 passes of EX-ECAP and (b) newly recrystallized small grains after 12 passes of EX-ECAP.

3

Thermal stability of the UFG structure investigated by EBSD

3.2. Thermal stability of the UFG structure investigated by EBSD

Microscopic techniques, in particular EBSD, can also contribute to the characterization of thermal stability of the UFG structure. The maintenance of the fine-grained structure is of particular importance for many physical properties, e.g., the superplasticity, etc. [23, 24].

Series of specimens for thermal stability investigation were prepared by isochronal annealing at the temperatures 150–500°C for 1 h followed by water-quench. The samples after extrusion and 4 passes of ECAP were chosen as suitable materials because of their UFG and homogeneous microstructure with relatively high dislocation density (see also Figure 8a).

The microstructure and grain size distribution of the specimen in the initial non-annealed condition after extrusion and 4 passes of ECAP are shown in Figure 16a and 16b, respectively. The microstructure is homogeneous comprising of very fine grains with an average size of 0.9 μm. The microstructure and grain sizes of the samples after 1 h of isochronal annealing at 150°C and 170°C (not shown here) are very similar to the non-annealed specimen.

Inhomogeneous grain growth is observed at higher annealing temperatures as displayed at Figure 17. Some grains start to grow at temperatures of 190°C (Figure 17a) and 210°C (not shown here). The fraction of coarse grains increases with increasing annealing temperature. At the temperature of 250°C, some areas with original fine grains are still observed, see Figure 17b. However, the small grains are continuously disappearing at higher annealing temperatures and nearly no small grains are observed after annealing at 400°C, see Figure 17e. Please

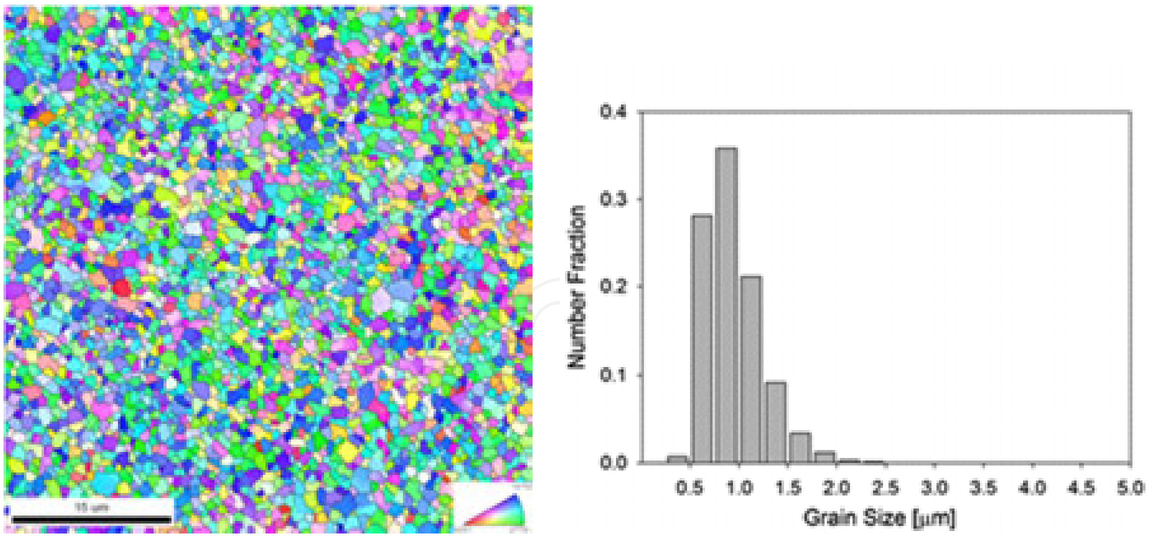

a) b)

Figure 16: Microstructure of the AZ31 sample after extrusion and 4 passes of ECAP, (a) inverse pole figure map and (b) grain size distribution.

Figure 16. Microstructure of the AZ31 sample after extrusion and 4 passes of ECAP, (a) inverse pole figure map and (b) grain size distribution.

Inhomogeneous grain growth is observed at higher annealing temperatures as displayed at Figure 17. Some grains start to grow at temperatures of 190°C (Figure 17a) and 210°C (not shown here). The fraction of coarse grains increases with increasing annealing temperature. At the temperature of 250°C, some areas with original fine grains are still observed, see Figure 17b. However, the small grains are continuously disappearing at higher annealing temperatures and nearly no small grains are observed after annealing at 400°C, see Figure 17e. Please note that magnification of Figure 17d and 17e is two times smaller than the magnification of the previous inverse pole figure maps; simultaneously, four times bigger area of the sample (100 × 100 µm) is depicted in Figure 17d and 17e. Microstructure of the specimens annealed at 450°C and 500°C was observed by light microscope and displayed in Figure 18

note that magnification of Figure 17d and 17e is two times smaller than the magnification of the previous inverse pole figure maps; simultaneously, four times bigger area of the sample (100 × 100 µm) is depicted in Figure 17d and 17e. Microstructure of the specimens annealed at 450°C and 500°C was observed by light microscope and displayed in Figure 18.

Grain size distribution and average grain size of the samples studied by EBSD were calculated from the data measured on the area 100 × 100 µm for all annealing temperatures to achieve better statistics. Statistical values from the samples studied by light microscopy were calculated from
two tha s intersecting
the sco analysis. The
dep ber is plotted in
Figu an culated from
the val mmarized in
Tab

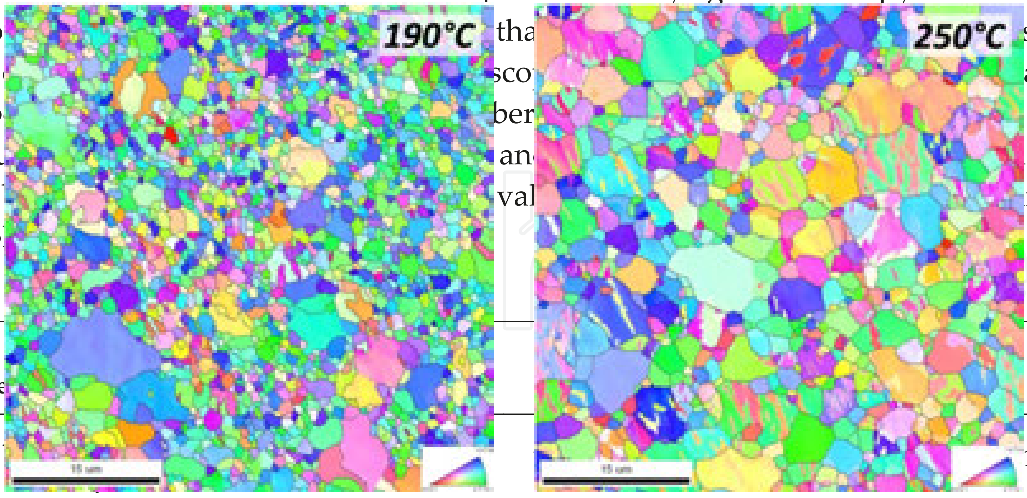

(a) (b)

te		
	450	500
	10.09	24.53

Table 2. The average grain sizes at different annealing temperatures.

Annealing twins observed after annealing at 250–400°C (see Figures 17b and 17e) were excluded from grain size calculations to achieve true grain size values (twin boundaries were ignored in grain size calculations, i.e., the twin is considered to be a part of the grain). All these fraction of coarse grains increases with increasing annealing temperature. At the temperature of 250°C, some areas with original fine grains are still observed, see Figure 17b. However, the small grains are continuously disappearing at higher annealing temperatures and nearly no small grains are observed after annealing at 400°C, see Figure 17e. Please note that magnification of Figure 17d and 17e is two times smaller than the magnification of the previous inverse pole figure maps; simultaneously, four times bigger area of the sample (100 × 100 µm) is depicted in Figure 17d and 17e. Microstructure of the specimens annealed at 450°C and 500°C was observed by light microscope and is displayed in Figure 18.

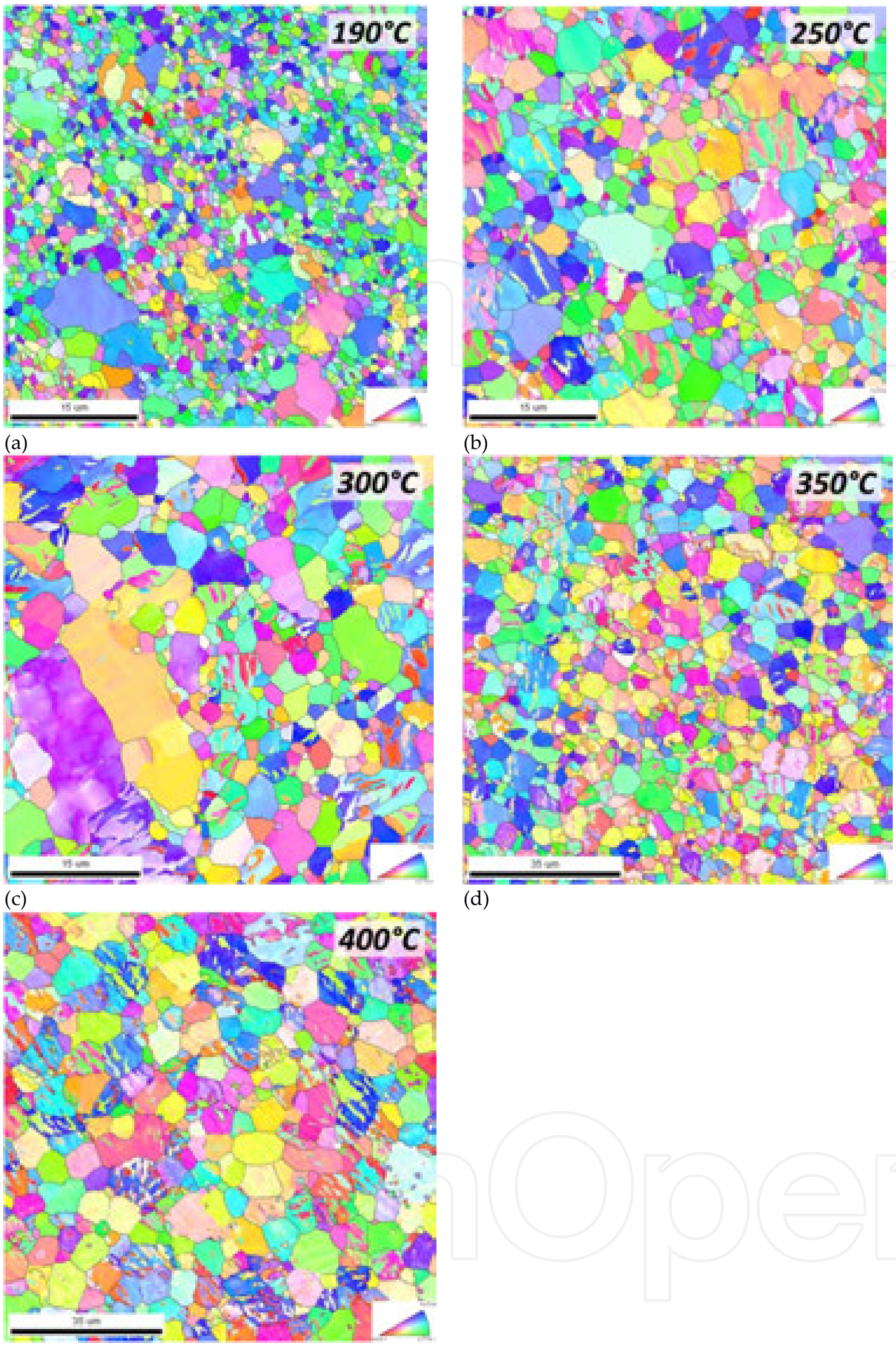

(a) (b) (c) (d) (e)

Figure 17: Microstructure of the AZ31 EX-ECAP specimen after 1 h of isochronal annealing at (a) 190°C,

Figure 17. Microstructure of the AZ31 EX-ECAP specimen after 1 h of isochronal annealing at (a) 190°C, (b) 250°C, (c) 300°C, (d) 350°C, and (e) 400°C (EBSD inverse pole figure maps).

twins were determined as the tensile twins with misorientation angle of 86° [25]. Twin fractions, fraction of twinned grains and the area fraction of twinned grains in samples after annealing at $T \geq 250$ °C are shown in Table 3.

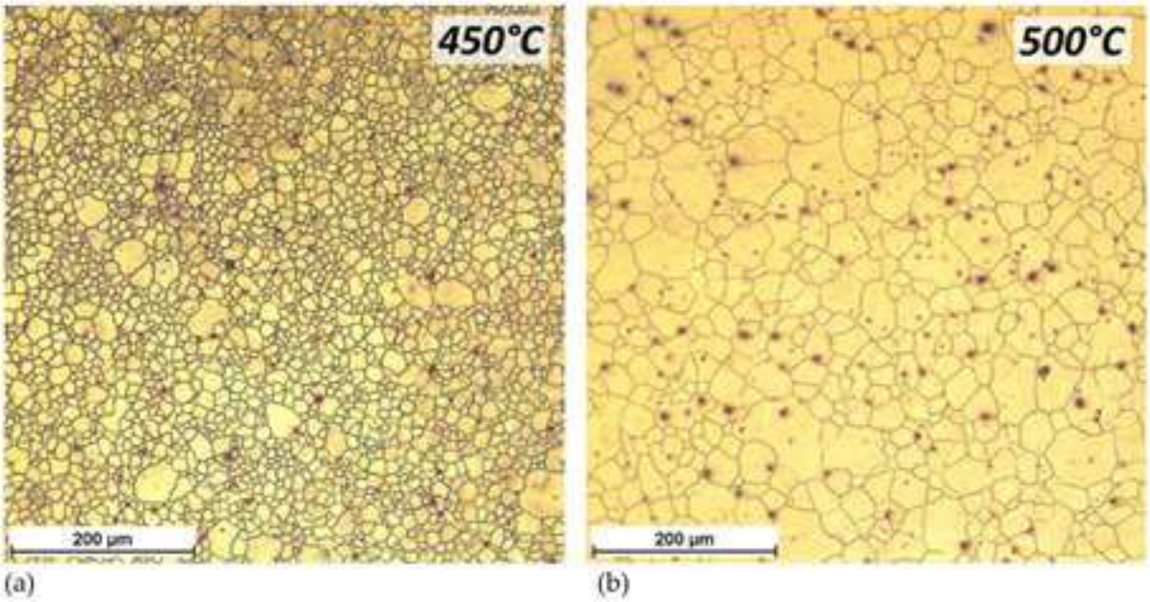

Figure 18. Microstructure of the AZ31 EX-ECAP specimen after 1 h of isochronal annealing at (a) 450°C and (b) 500 °C (light microscope images).

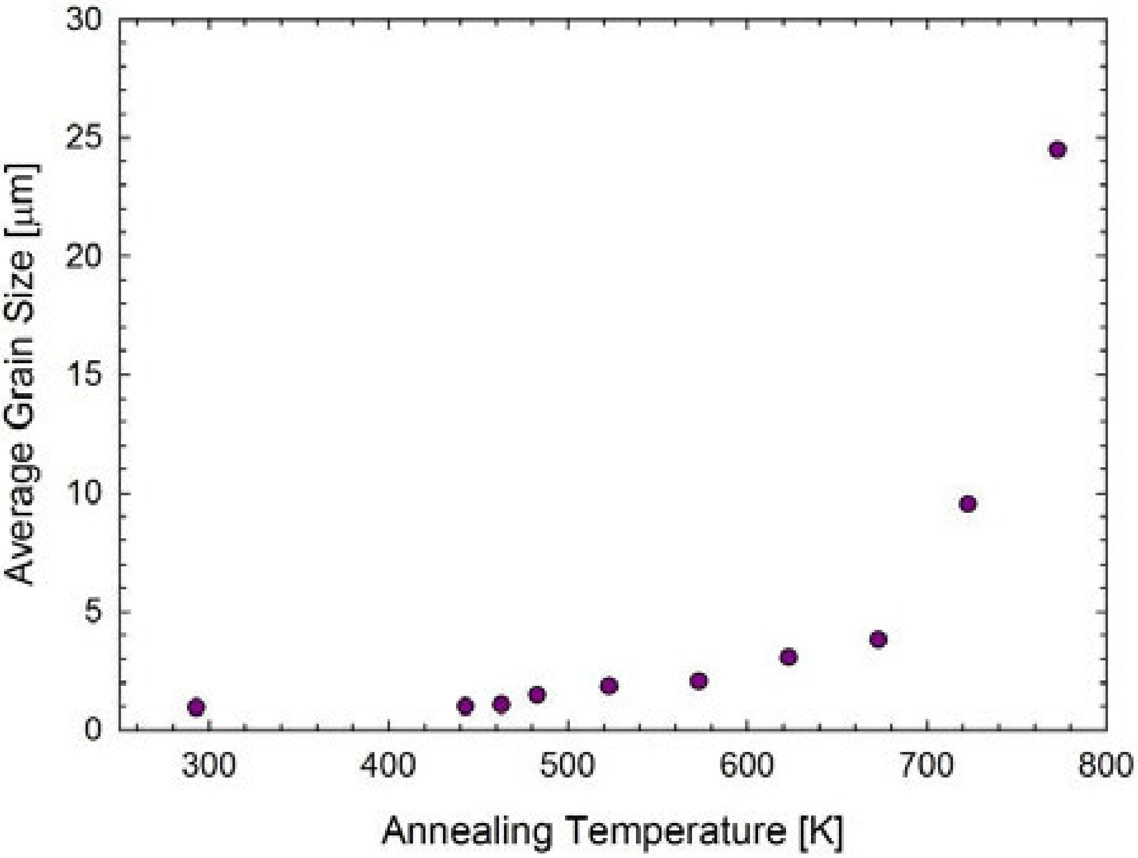

Figure 19. Dependence of the average grain size (number average, excluding twins) of the EX-ECAP AZ31 alloy on annealing temperature after 1 h of isochronal annealing process.

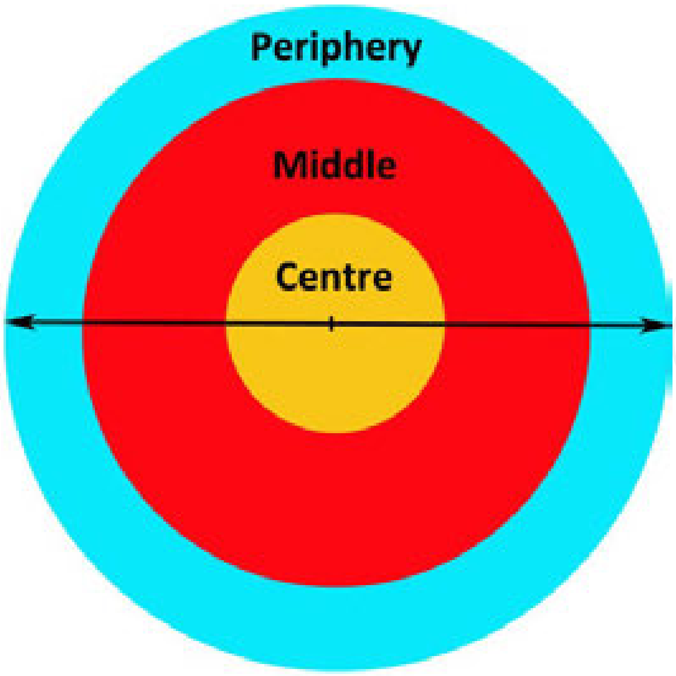

Figure 20. Schematic illustration of three different parts of the disks processed by HPT.

Annealing Temperature	250°C	300°C	350°C	400°C
Twin Fraction	0.13	0.12	0.16	0.14
Fraction of Twinned Grains	0.26	0.26	0.37	0.40
Area Fraction of Twinned Grains	0.55	0.52	0.60	0.71

Table 3. Twinning in isochronally annealed EX-ECAP AZ31 alloy.

3.3. Microstructure evolution in UFG AZ31 processed by HPT investigated by ACOM-TEM

The microstructure of the materials after SPD cannot be often observed by light microscopy because of their very small grain sizes. EBSD is usually a much better and suitable method in this case. However, even EBSD has some limitation in resolution or some "more local" method could be required for microstructure observations. This often occurs in specimens processed by high pressure torsion. This method proved to be more effective in grain refinement than the ECAP due to mainly much larger strains imposed on the HPT disk during processing and also lower temperatures of processing as compared to ECAP [2, 9]. TEM is a well-known technique that usually solves the problem. ACOM-TEM is a very sophisticated method, alternative to EBSD, which enables to study extremely fine-grained materials. We used this technique for microstructure observations of the most deformed parts of HPT specimens. Due to the inhomogeneous character of strain imposed to the material by HPT, disks processed by HPT could be divided into three parts: center, middle, and periphery (see Figure 20).

Due to relatively low imposed strain after one HPT rotation, EBSD is sufficient to be employed for microstructure observation. Figures 21a and 21b show deformed microstructures of the central and middle parts of the specimen after 1 turn studied by EBSD. The areas investigated by EBSD could be relatively big—in our case it was the area 100 × 100 µm. The step size of these measurements was 100 nm. Figure 21a displays a heavily deformed microstructure of the central part of the specimen with a lot of multiple twinning. The microstructure of the middle part of the sample after 1 HPT rotation, shown in Figure 21b, consists of several large elongated grains with no twins and a lot of new grains of the average size of few microns.

The same middle part of this specimen was studied using ACOM-TEM and the typical results are displayed in Figure 22a. Measurements were done with step size 20 nm, which is five times smaller than the step size of the EBSD measurements. ACOM-TEM measurements confirmed heterogeneous microstructures with large elongated grains and a lot of small grains. The microstructure of the peripheral part (see Figure 22b) is homogeneous with very small grains only (≈ 100–300 nm).

The same middle part of this specimen was studied using ACOM-TEM and the typical results are displayed in Figure 22a. Measurements were done with step size 20 nm, which is five times smaller than the step size of the EBSD measurements. ACOM-TEM measurements confirmed heterogeneous microstructures with large elongated grains and a lot of small grains. The microstructure of the peripheral part (see Figure 22b) is homogeneous with very small grains only (≈ 100–300 nm).

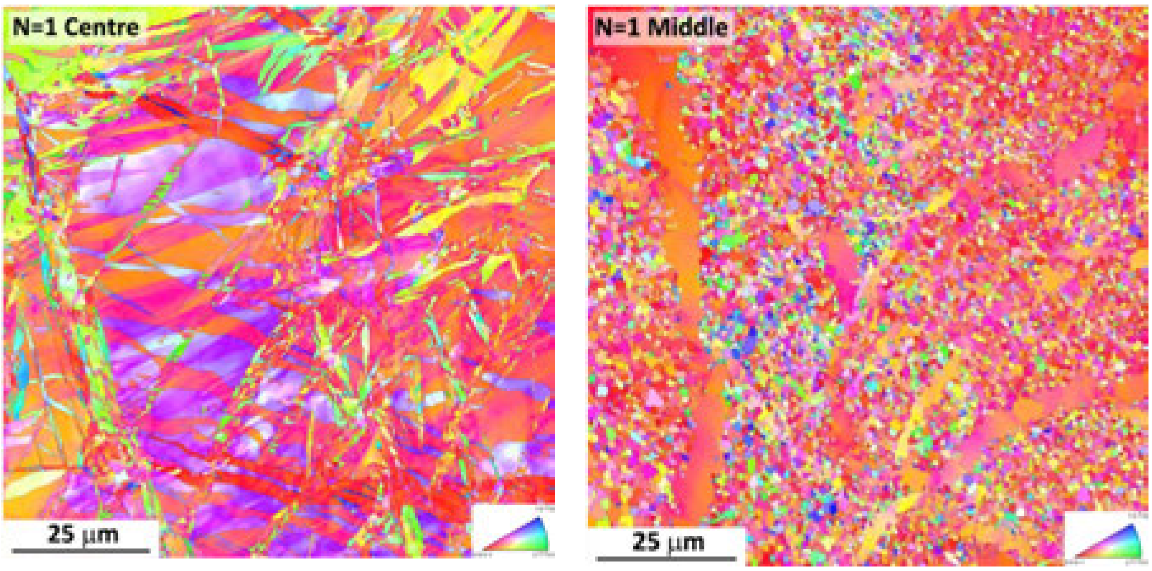

(a) (b)

Figure 21: EBSD IPF image of microstructure of the AZ31 sample after 1 turn of HPT, (a) central part and (b) middle part

Figure 21. EBSD IPF image of microstructure of the AZ31 sample after 1 turn of HPT, (a) central part and (b) middle part.

The sample, after 5 turns of HPT, was investigated using ACOM-TEM in the middle and the peripheral part of the disk. The microstructure of the middle part (see Figure 23a) is comparable with the middle part of the sample after 1 HPT rotation; it consists of large elongated deformed grains and a lot of small grains surrounding the bigger grains. The microstructure of the peripheral part of the disk after 5 HPT turns, shown in Figure 23b, is composed mainly of very small grains. However, few remaining grains with the size of several microns could be still observed in the peripheral part. The ACOM-TEM is a very local method where the relatively small part of a thin foil could be investigated. Thus, the statistics of measurements of heterogeneous microstructure is not sufficient. Preparation and investigation of more TEM foils is needed to improve the statistics (despite each image consisting of observations at four different zones of a foil).

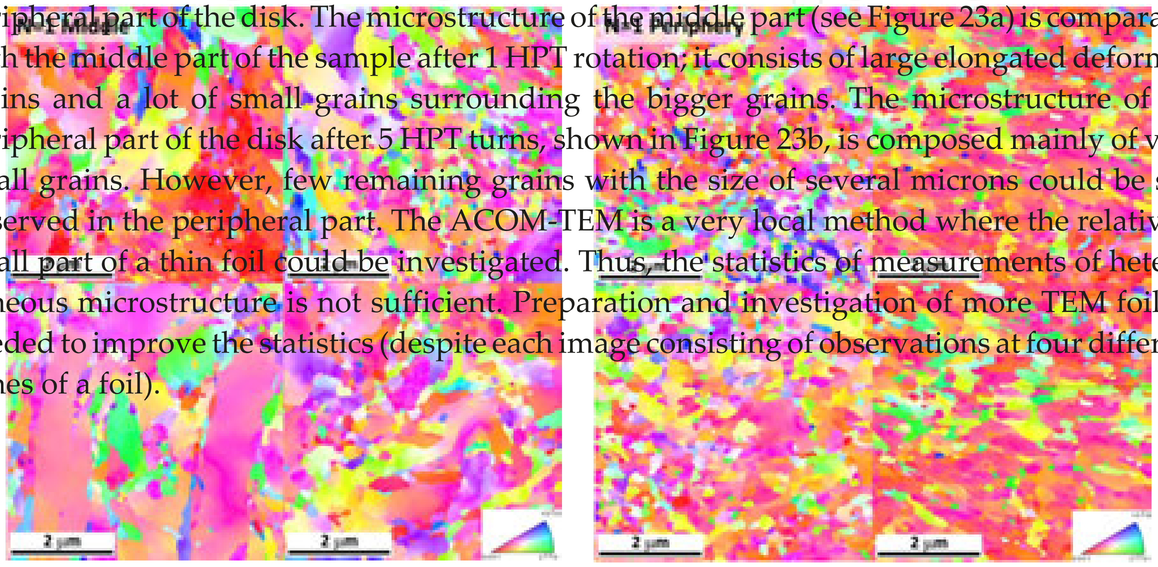

(a) **(b)**

Figure 22: ACOM-TEM image of the microstructure of the AZ31 sample after 1 turn of HPT, (a) middle part and (b) periphery.

is five times smaller than the step … ACOM-TEM measurements confirmed heterogeneous microstru… lot of small grains. The microstructure of the peripheral part (see … all grains only (≈ 100–300 nm).

Figure 21: EBSD IPF image of microstructure of the AZ31 sample after 1 turn of HPT, (a) central part and (b) middle part.

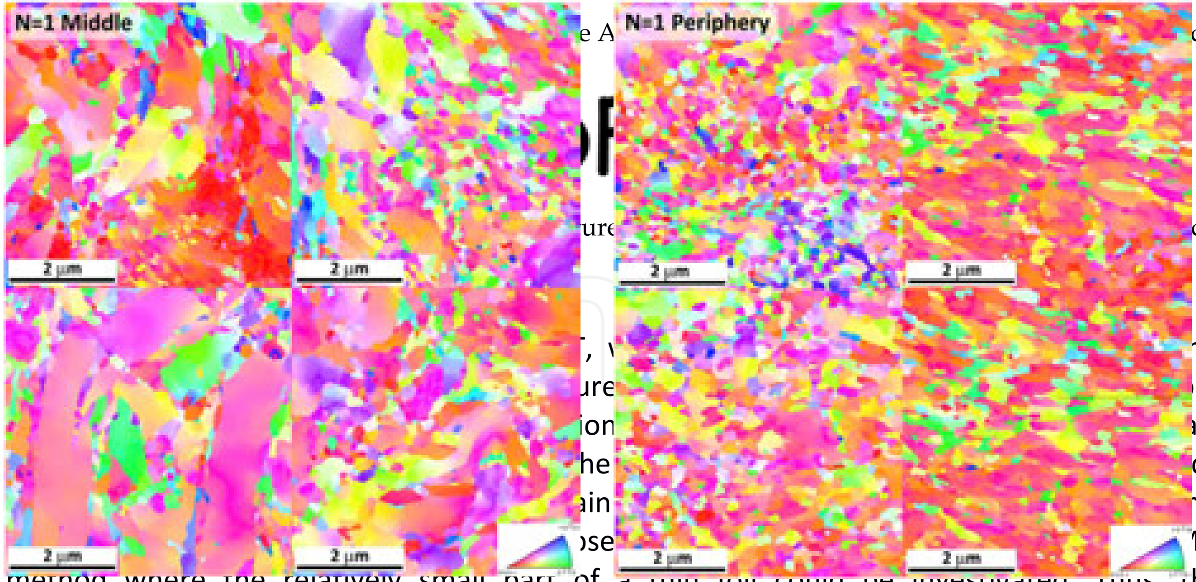

(a) (b)

method where the relatively small part of a thin foil could be investigated. Thus, the statistics of measurements of heterogeneous microstructure is not sufficient. Preparation and investigation of more TEM foils is needed to improve the statistics (despite each image consisting of observations at four different zones of a foil).

Figure 22. ACOM-TEM image of the microstructure of the AZ31 sample after 1 turn of HPT, (a) middle part and (b) periphery.

Figure 22: ACOM-TEM image of the microstructure of the AZ31 sample after 1 turn of HPT, (a) middle part and (b) periphery.

The sample, after 5 turns of HPT, was investigated using ACOM-TEM in the middle and the peripheral part of the disk. The microstructure of the middle part (see Figure 23a) is comparable with the middle part of the sample after 1 HPT rotation; it consists of large elongated deformed grains and a lot of small grains surrounding the bigger grains. The microstructure of the peripheral part of the disk after 5 HPT turns, shown in Figure 23b, is composed mainly of very small grains. However, few remaining grains with the size of several microns could be still observed in the peripheral part. The ACOM-TEM is a very local method where the relatively small part of a thin foil could be investigated. Thus, the statistics of measurements of heterogeneous microstructure is not sufficient. Preparation and investigation of more TEM foils is needed to improve the statistics (despite each image consisting of observations at four different zones of a foil).

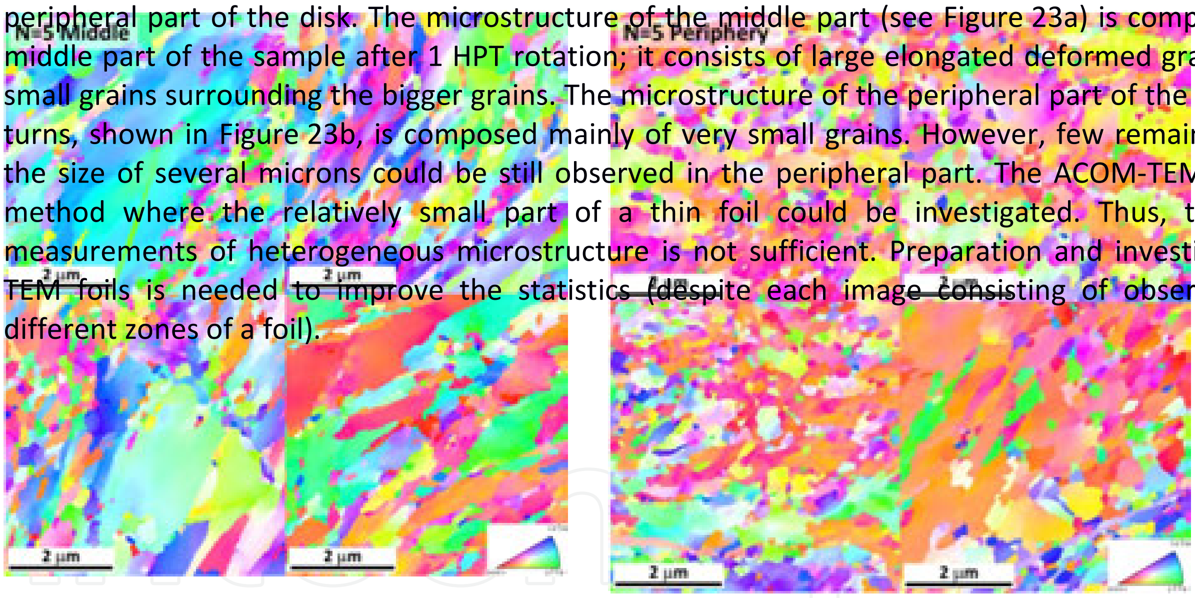

(a) (b)

Figure 23: ACOM-TEM image of the microstructure of the AZ31 sample after 5 turns of HPT, (a) middle part and (b) periphery.

Figure 23: ACOM-TEM image of the microstructure of the AZ31 sample after 5 turns of HPT, (a) middle part and (b) periphery.

Figures 24a and 24b display the microstructure of the middle and peripheral part of the disk after 15 HPT rotations, respectively. The microstructure of both parts is more homogeneous than the microstructure of the same parts of the disk after 5 HPT turns.

Figures 24a and 24b display the microstructure of the middle and peripheral part of the disk after 15 HPT rotations, respectively. The microstructure of both parts is more homogeneous than the microstructure of the same parts of the disk after 5 HPT turns.

Grain size distributions of extremely fine grained microstructure of the peripheral parts of the disks after 1 and 15 HPT rotations (see Figure 25) show that about 60%, and nearly 70%, of

Figure 23: ACOM-TEM image of the microstructure of the AZ31 sample after 5 turns of HPT, (a) middle part and (b) periphery.

Figures 24a and 24b display the microstructure of the middle and peripheral part of the disk after 15 HPT rotations, respectively. The microstructure of both parts is more homogeneous than the microstructure of the same parts of the disk after 5 HPT turns.

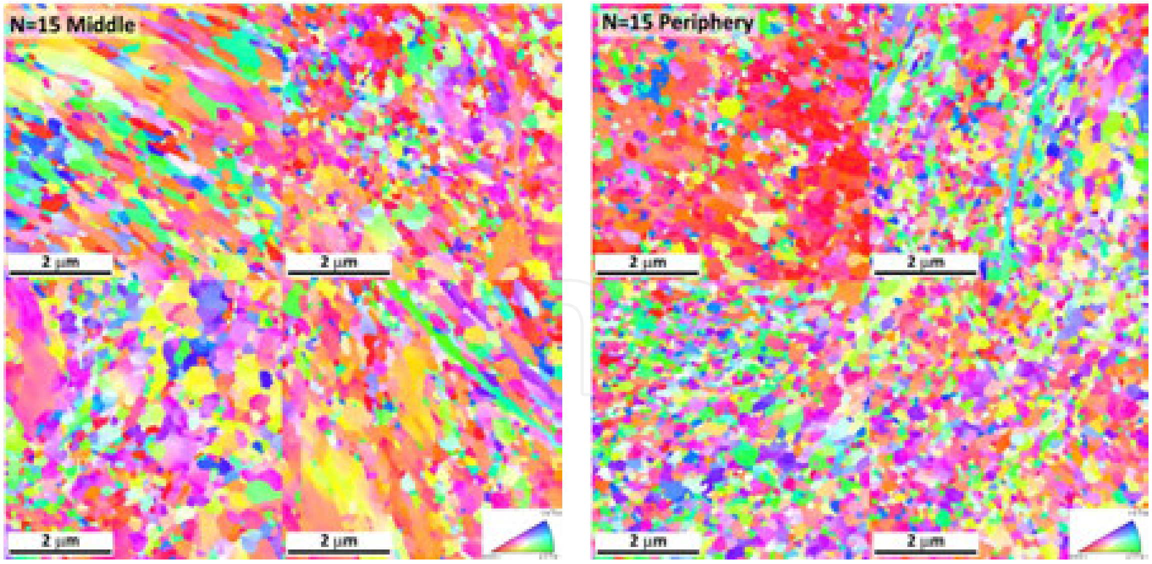

(a) (b)

Figure 24: ACOM-TEM image of the microstructure of the AZ31 sample after 15 turns of HPT, (a) middle

Figure 24. ACOM-TEM image of the microstructure of the AZ31 sample after 15 turns of HPT, (a) middle part and (b) periphery.

grains, respectively, have a diameter of 100–200 nm that proves clearly the efficiency of grain refinement by HPT.

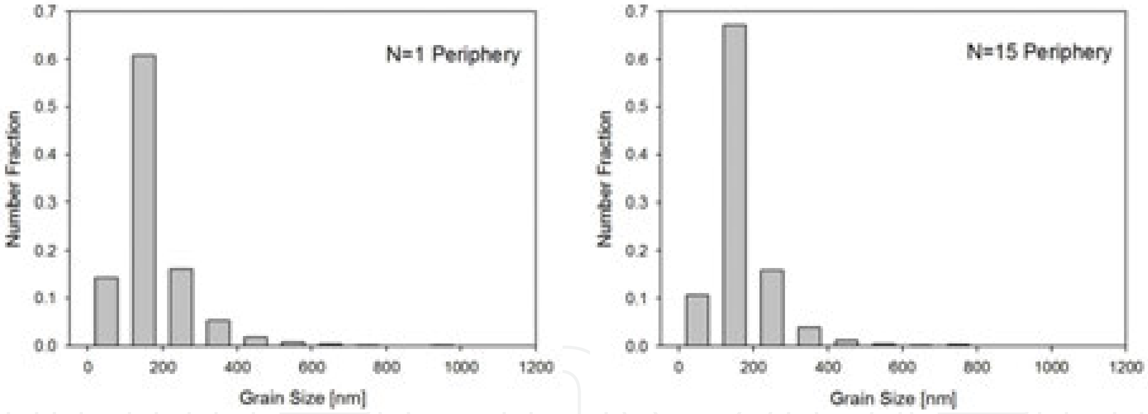

a) b)

Figure 25: Grain size distribution of the peripheral part of the disk after (a) 1 and (b) 15 rotations of HPT.

Figure 25. Grain size distribution of the peripheral part of the disk after (a) 1 and (b) 15 rotations of HPT.

4 Conclusions

4. Conclusions

Microstructure evolution in ultra-fine grained magnesium alloy AZ31 prepared by severe plastic deformation was investigated by several experimental techniques. The following conclusions may be drawn from this investigation:

Microstructure evolution in ultra-fine grained magnesium alloy AZ31 prepared by severe plastic deformation was investigated by several experimental techniques. The following conclusions may be drawn from this investigation:

- Due to limited resolution light microscopy may be employed to investigate the initial stages of grain fragmentation, i.e., the specimens processed by low number of ECAP passes or low number of HPT turns and especially in zones around the disk centers;
- EBSD proved to be a very powerful technique for the investigation of various stages of grain refinement. It allows to characterize not only the grain fragmentation, but also to determine other microstructural features as the grain size distribution and the grain boundary character distribution (the fraction of LAGBS vs. HAGBs), as well as the texture evolution with strain imposed to the material by ECAP and/or HPT;
- TEM allows to characterize the details of the microstructure, namely the dislocation arrangements, grain boundary character (equilibrium vs. nonequilibrium grain boundaries), twins, twin and other special boundaries, etc.;
- The special technique of ACOM-TEM may be used to characterize the terminal stages of grain

- Due to limited resolution light microscopy may be employed to investigate the initial stages of grain fragmentation, i.e., the specimens processed by low number of ECAP passes or low number of HPT turns and especially in zones around the disk centers;
- EBSD proved to be a very powerful technique for the investigation of various stages of grain refinement. It allows to characterize not only the grain fragmentation, but also to determine other microstructural features as the grain size distribution and the grain boundary character distribution (the fraction of LAGBS vs. HAGBs), as well as the texture evolution with strain imposed to the material by ECAP and/or HPT;
- TEM allows to characterize the details of the microstructure, namely the dislocation arrangements, grain boundary character (equilibrium vs. nonequilibrium grain boundaries), twins, twin and other special boundaries, etc.;
- The special technique of ACOM-TEM may be used to characterize the terminal stages of grain refinement (saturation) with grain sizes approaching to nanometer range (grain size < 100 nm), which is typical for peripheral zones of specimens processed by multiple turns of HPT;
- Complex microstructure characterization by different techniques of electron microscopy allows to understand the microscopic mechanisms of grain refinement, grain fragmentation, structure stability, as well as other important properties of ultra-fine grained materials processed by severe plastic deformation.

Acknowledgements

This work was financially supported by the Czech Science Foundation under the project GB14-36566G.

Author details

Jitka Stráská, Josef Stráský, Peter Minárik, Miloš Janeček* and Robert Král

*Address all correspondence to: janecek@met.mff.cuni.cz

Charles University in Prague, Department of Physics of Materials, Prague, Czech Republic

References

[1] Gupta M, Sharon NML. Magnesium, Magnesium Alloys, and Magnesium Composites. 1st ed. Wiley; 2011.

[2] Langdon TG. Twenty-five years of ultrafine-grained materials: Achieving exceptional properties through grain refinement. Acta Mater. 2013;61:7035–7059. DOI: 10.1016/j.actamat.2013.08.018.

[3] Estrin Y, Vinogradov A. Extreme grain refinement by severe plastic deformation: A wealth of challenging science. Acta Mater. 2013;61:782–817. DOI: 10.1016/j.actamat.2012.10.038.

[4] Horita Z, Matsubara K, Makii K, Langdon TG. A two-step processing route for achieving a superplastic forming capability in dilute magnesium alloys. Scr. Mater. 2002;47:255–260. DOI: 10.1016/S1359-6462(02)00135-5.

[5] Matsubara K, Miyahara Y, Horita Z, Langdon TG. Developing superplasticity in a magnesium alloy through a combination of extrusion and ECAP. Acta Mater. 2003;51:3073–3084. DOI: 10.1016/S1359-6454(03)00118-6.

[6] Gubicza J, Chinh NQ, Dobatkin SV, Khosravi E, Langdon TG. Stability of Ultrafine-Grained Microstructure in Fcc Metals Processed by Severe Plastic Deformation. Key Eng. Mater. 2011;465:195–198. DOI: 10.4028/www.scientific.net/KEM.465.195.

[7] Segal VM, Reznikov VI, Drobyshevskiy AE, Kopylov VI. Plastic working of metals by simple shear. Russ. Metall. 1981;1:99.

[8] Iwahashi Y, Wang J, Horita Z, Nemoto M, Langdon TG. Principle of equal-channel angular pressing for the processing of ultra-fine grained materials. Scr. Mater. 1996;35:143–146. DOI: 10.1016/1359-6462(96)00107-8.

[9] Zhilyaev AP, Langdon TG. Using high-pressure torsion for metal processing: Fundamentals and applications. Prog. Mater. Sci. 2008;53:893–979. DOI: 10.1016/j.pmatsci.2008.03.002.

[10] Kuznetsov RI, Bykov VI, Chernyshev VP, Pilyugin VP, Yefremov NA, Pasheyev AV. Plastic Deformation of Solid Bodies Under Pressure: 1. Equipment and Methods. Preprint 4/85, Sverdlovsk: IFM UNTs AN SSSR; 1985.

[11] Song Y, Yoon EY, Lee DJ, Lee JH, Kim HS. Mechanical properties of copper after compression stage of high-pressure torsion. Mater. Sci. Eng. A. 2011;528:4840–4844. DOI: 10.1016/j.msea.2011.02.020.

[12] Degtyarev MV, Chashchukhina TI, Voronova LM, Patselov AM, Pilyugin VP. Influence of the relaxation processes on the structure formation in pure metals and alloys under high-pressure torsion. Acta Mater. 2007;55:6039–6050. DOI: 10.1016/j.actamat.2007.04.017.

[13] Lee DJ, Yoon EY, Park LJ, Kim HS. The dead metal zone in high-pressure torsion. Scr. Mater. 2012;67:384–387. DOI: 10.1016/j.scriptamat.2012.05.024.

[14] Kim HS. Finite element analysis of high pressure torsion processing. J. Mater. Process. Technol. 2001;113:617–621. DOI: 10.1016/S0924-0136(01)00709-9.

[15] Yoon SC, Horita Z, Kim HS. Finite element analysis of plastic deformation behavior during high pressure torsion processing. J. Mater. Process. Technol. 2008;201:32–36. DOI: 10.1016/j.jmatprotec.2007.11.204.

[16] Vrátná J. Physical Properties of Ultrafine-grained Polycrystals of Magnesium Based Alloys [thesis]. Prague: Charles University in Prague; 2010.

[17] Williams DB, Carter CB. Transmission Electron Microscopy: A Textbook for Materials Science. 2nd ed. New York: Springer, 2009. ISBN 9780387765020.

[18] Schwarzer RA, Zaefferer S. An Inexpensive CCD Camera System for the Recording and On-Line Interpretation of TEM Kikuchi Patterns. Mater. Sci. Forum. 1994;157-162:189–194. DOI: 10.4028/www.scientific.net/MSF.157-162.189.

[19] Rauch EF, Veron M. Coupled microstructural observations and local texture measurements with an automated crystallographic orientation mapping tool attached to a TEM. Mater. Werkst. 2005;36:552–556. DOI: 10.1002/mawe.200500923.

[20] Rauch EF, Dupuy L. Rapid spot diffraction patterns idendification through template matching. Arch. Metall. Mater. 2005;50:87–99.

[21] Bohlen J, Yi SB, Swiostek J, Letzig D, Brokmeier HG, Kainer KU. Microstructure and texture development during hydrostatic extrusion of magnesium alloy AZ31. Scr. Mater. 2005;53:259–264. DOI: 10.1016/j.scriptamat.2005.03.036.

[22] Agnew SR, Mehrotra P, Lillo TM, Stoica GM and Liaw PK. Crystallographic texture evolution of three wrought magnesium alloys during equal channel angular extrusion. Mater. Sci. Eng. A. 2005;408:72–78. DOI: 10.1016/j.msea.2005.07.052.

[23] Valiev RZ, Islamgaliev RK, Alexandrov IV. Bulk nanostructured materials from severe plastic deformation. Prog. Mater. Sci. 2000;45:103–189. DOI: 10.1016/S0079-6425(99)00007-9.

[24] Valiev RZ, Estrin Y, Horita Z, Langdon TG, Zechetbauer MJ, Zhu YT. Producing bulk ultrafine-grained materials by severe plastic deformation. JOM. 2006;58:33–39. DOI: 10.1007/s11837-006-0213-7.

[25] Aghababaei R, Joshi SP. Micromechanics of tensile twinning in magnesium gleaned from molecular dynamics simulations. Acta Mater. 2014;69:326–342. DOI: 10.1016/j.actamat.2014.01.014.